# CHALMERS



# Micromechanical modeling of dual-phase steels

Master's thesis in Structural Engineering and Building Technology

ANTONIA RAMBÖL BRYNTESSON

MASTER'S THESIS IN STRUCTURAL ENGINEERING AND BUILDING TECHNOLOGY

# Micromechanical modeling of dual-phase steels

ANTONIA RAMBӦL BRYNTESSON

Micromechanical modeling of dual-phase steels
Master's thesis in Structural Engineering and Building Technology
ANTONIA RAMBÖL BRYNTESSON
Department of Industrial and Materials Science
Division of Material and Computational Mechanics
Chalmers University of Technology

# ABSTRACT

Dual-phase (DP) steel is a high strength steel, much used by the automotive industry due to its characteristic combination of low initial yield stress, high tensile stress and easy cold working and weldability. These advantageous features are related to the microstructure of soft ferrite and hard martensite. The total mechanical behavior of such a material is primarily derived from the volume fraction of each phase, grain sizes, distribution of the phases and alloying elements. However, to be able to benefit from the prominent features of the material to an even greater extent than today, more knowledge on how the microstructural parameters are correlated to its end-properties is needed.

In this thesis the mechanical behavior of DP steel in uniaxial tension is studied with regard to microstructure. A micromechanical modeling framework utilizing an axisymmetric representative volume element (RVE) is implemented in Abaqus. The RVE consists of a sphere representing the martensite, in a cylinder of ferrite. A single-phase material model describing the plastic flow is applied to each respective phase, but with different material parameters. This constitutive description is developed from a dislocation density theory where microstructural parameters control the plastic flow. More knowledge about the behavior of the DP steel, the microstructure, correlations between different parameters, modeling techniques and constitutive models suitable for DP steels were retrieved from a literature review.

Microstructural characterization and mechanical testing in tensile response and hardness have previously been performed on four DP steels in varying strength classes at the Norwegian University of Science and Technology. The retrieved microstructural data was applied to the micromechanical model and the results from the mechanical testing were used to validate the predictions on tensile response from numerical simulations of the micromechanical model.

Despite the simplicity of the micromechanical modelling framework it in general produces results that are in good agreement with the corresponding mechanical tests. However, deviations are seen in the modeling of the strongest steel, which has the highest volume fraction of martensite. This may indicate that the ferrite is more accurately represented than the martensitic phase. It was also shown that when the geometry of the martensitic sphere was changed in such a way that the ferrite in certain areas got more constrained, an undesired strengthening effect was obtained. This indicates that the specific RVE used in the study has geometrical limitations and that it is more suitable for lower volume fractions of martensite.

The thesis has been conducted through a collaboration between Chalmers University of Technology and Norwegian University of Science and Technology.

Keywords: Dual-phase steel, Micromechanical modeling, Representative volume element (RVE), Ferrite, Martensite

# Preface

The thesis herein presented is an outcome of six months of work and concludes a Master's degree in Structural Engineering after five years of studies. The project was empowered from a collaboration between Chalmers University of Technology and Norwegian University of Science and Technology (NTNU). The thesis was conducted at the Centre for Advanced Structural Analysis at the Department of Structural Engineering at NTNU but evaluated and within the frames set by Chalmers. Several persons have been involved in the progress of the project, whom I would like to express my sincerely gratitude to.

- My supervisors Professor Tore Børvik and Professor Odd Sture Hopperstad at NTNU. We had weekly meetings where my questions were answered with their comprehensive theoretical knowledge and the guidance of the proceeding work have been decisive for the outcome of these months.

- My examiner Professor Magnus Ekh at Chalmers. He has been a great support and made sure that the thesis has been conducted according to the university standards.

- PhD Candidate Christian Oen Paulsen for providing me with the microstructural data and results from hardness tests. He has also provided back support in the parts related to microstructural characterization.

- Postdoctoral Fellow Maria Jesus Perez for introducing me to the work that had already been performed on the DP steel at the department and for sharing her results from the tensile tests on the four DP steels.

- Research Scientist Afaf Saai at SINTEF for sharing her conducted work on DP steels.

The project has been very interesting all the way. I have been exposed to many new methods and tools that I certainly will benefit from in my future professional life. I hope this thesis will add to the knowledge of others interested in DP steels.

# Contents

CHAPTER 1

---

Introduction

---

## 1.1  Background and motivation

Dual phase steel (DP steel) is a part of the Advanced High Strength Steels (AHSS) and has been developed continuously during the last decades. The microstructure, consisting of a ferritic matrix with dispersed islands of martensite, gives the material an outstanding combination of strength and ductility. The ferrite contributes to ductility while the martensite reinforces the material. The interaction between the two phases and with the strain being concentrated to the continuous ferrite surrounding the hard martensite give rise to an initial high strain hardening, thus producing great drawability. The combination of these features makes the steel ideal for use in the automotive industry. Passenger safety, weight reduction, vehicle performance and fuel efficiency are some of the benefits accompanied with introducing DP steels into cars.

Both the intrinsic properties of each phase as well as microstructural features such as the volume fractions of the phases and grain sizes affect the macrostructural behavior of the steel. The complexity of the microstructure and the large number of parameters affecting the end-properties make it a challenge to design a steel with the requirements needed for specific structural applications. Hence, many scientific researchers have recently focused on combining experimental mechanical techniques with numerical micromechanical models in order to gain knowledge on the relationship between properties and structure.

By use of digital image correlation and in-situ scanning electron microscopy, four different DP steels (DP500, DP600, DP800 and DP980) have previously been studied at the Department of Structural Engineering at the Norwegian University of Technology. In this thesis a micromechanical model is established in order to investigate the combination of mechanical behavior and parameters that are needed to predict the response of the four DP steels.

## 1.2    Thesis objective

The aim of the project is to develop a better understanding for how the mechanical behavior of DP steels is affected by microstructural factors. To achieve this, a microstructure-based finite element modeling framework will be applied in large-scale simulations of DP steels using Abaqus. Both the distribution of the phases and their individual constitutive behaviors will be studied.

The work includes:

- Literature study on the microstructure, mechanical behavior, and microstructure-based modeling and simulation of DP steels.

- Evaluation of previously conducted experimental results towards model adaptation.

- Implementation and evaluation of the microstructure-based finite element modeling framework in Abaqus through simulation of the stress-strain behavior of DP steel.

- Parametric study on the influence of microstructural features on the stress-strain behavior of DP steels.

## 1.3    Limitations

The study is confined regarding some aspects. The limitations are:

- No 2D-model and no models based on real microstructures are studied.

- The description of the work-hardening is restricted to a physically based model, excluding models based on empirical equations.

- Yield criterion when modeling plasticity is restricted to von Mises yield criterion. At the end of the thesis, ductile fracture is studied with a Gurson-Tvergaard-Needleman yield criterion.

- Parameters studied in the description of the flow stress are the ferrite grain size, $d_f$, the carbon content in both martensite, $C_m$, and ferrite, $C_f$, the constants, $P_1$ and $P_2$, in the relation describing solid solution strengthening from carbon in martensite and also indirectly, through $d_f$, the parameter describing dynamic recovery, $k_r$ and dislocation mean free path $L_f$ since they both are set to depend on $d_f$.

- The model is only validated with regard to uniaxial tension.

Essential Theory

In this chapter some basic theory is presented and definitions used throughout the thesis are defined. The selection of included subjects are based on two aspects. First: the central parts of the thesis. Thus, the tensile test, Section 2.1.1, due to the choice of studied loading condition, and work-hardening, Section 2.1.2, because the description of the plastic flow is one of the major concerns in the study. Second: the previous knowledge of the author. Hence, the parts about ductile fracture, Section 2.1.3 and metallurgy, Section 2.2 are comparatively comprehensive.

## 2.1   Materials Mechanics

### 2.1.1   The tensile test

One of the most fundamental approaches to determine the mechanical properties of a material is to perform a tensile test. A specimen of standardized geometry is loaded until fracture. The deformation rate is pre-set while the load and elongation is traced. With data on force and displacement, a stress-strain curve can be constructed.

In Figure 2.1.1 a typical stress-strain curve is shown. The initial straight part of the curve, is the linear elastic part. The slope of the curve gives the value of Young's modulus for isotropic materials. As the slope of the curve changes, the elastic limit is reached and upon unloading, the deformation is no longer recoverable, a permanent strain in the specimen is obtained. This limit corresponds to the yield stress. The maximum stress, at the top of the curve, is the ultimate tensile strength. At this point, a phenomena known as necking occurs where the deformation goes from being uniformly distributed across the gauge of the specimen to localize in more confined regions. Finally the specimen breaks and the total elongation to fracture is obtained [36].

Typical measures retrieved from the tensile test:

- The elastic stiffness (or Young's modulus), which is a measure of a material's behavior during elastic deformation.

- The initial yield stress (or strength), which is a measure of a material's elastic capacity. A typical reported value for the initial yield stress is at 0.2% plastic strain and is known as the proof stress.

- The ultimate tensile stress (or strength), which measures a material's maximum load bearing capacity during plastic deformations.

- Total elongation to fracture, which is a measure of ductility.

The engineering strain and stress are defined as:

$$\varepsilon_{eng} = \frac{L - L_0}{L_0} \tag{2.1.1a}$$

$$\sigma_{eng} = \frac{F}{A_0} \tag{2.1.1b}$$

Where $L_0$ and $A_0$ are the initial gauge length and initial cross sectional area, respectively. This is illustrated in Figure 2.1.2 where a bar is loaded in uniaxial tension and $L = L_0 + \Delta L$. The engineering stress and strain measures are based on the initial cross-sectional area and gauge length and are commonly used measures due to the ease of data extraction during experiments. However, the engineering stress-strain curve does not give a complete description of the deformation characteristics since the geometry of a material may change significantly during deformation. For large deformations true stress and strain is a better option of measures. True stress and strain take changes in cross sectional area into consideration by using an instantaneous area [36].

By assuming neglectable elastic strains and isochoric plastic deformations (i.e. no change in volume), the conversion from engineering to true strain and stress is obtained from the following:

$$\varepsilon_{true} = ln(\frac{L}{L_0}) \tag{2.1.2a}$$

$$\sigma_{true} = \frac{F}{A} = \frac{\sigma_{eng}(1 + \varepsilon_{eng})}{A} \tag{2.1.2b}$$

### 2.1.2   Work hardening

As a material is subjected to plastic deformation it hardens and the strength of the material is increased. The yield function $g$, defined in Equation 2.1.3 where $\sigma_0$ is the yield stress and $\varphi(\sigma_{ij}) = \sigma_{eq}$ is the equivalent stress measuring the magnitude of the stress state to which the material is subjected to, is no longer only dependent on the stress [25].

$$g(\sigma) = \varphi(\sigma_{ij}) - \sigma_0 \tag{2.1.3}$$

The work hardening can be accounted for in the yield function if one let the yield stress depend on plastic straining. This is called isotropic hardening, which is one of the two most common ways to account for work-hardening. The second is kinematic hardening, however, in this
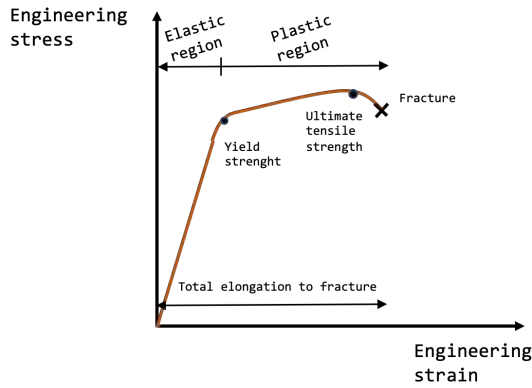
Figure 2.1.1: *Schematic stress vs. strain curve. Based on figure from [36]*
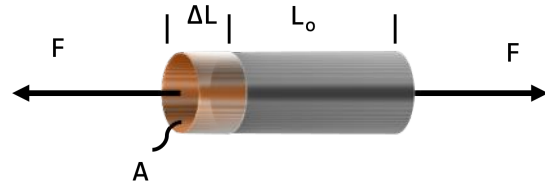


Figure 2.1.2: *Bar loaded in uniaxial tension. Based on figure from [36]*

thesis only isotropic hardening will be considered, hence kinematic hardening is not further discussed. With isotropic work hardening the elastic region expands in the plastic domain during deformation, but without changing the form or translating the centre of the region. The isotropic work hardening is accounted for in the yield function as [25]:

$$g = \varphi(\sigma_{ij}) - (\sigma_0 + R) = 0 \tag{2.1.4}$$

Where $\sigma_0 + R$ is the flow stress of the material. As the material is deformed in the plastic region, both the hardening variable and the flow stress increases [25]. In this work, the model describing the flow stress will be referred to as the single phase material model and is a physically based model emerging from dislocation based theory.

From a physical perspective work hardening can be described as when stresses are exerted on the material, crystals slip against each other. These slips are known as dislocations, and initially decrease the strength of the material. However, as these dislocations accumulate they tend to work as obstacles for further slips. This complex interaction manifests as work hardening on a macroscopic level in the material. The ability to deform plastic depends on the degree to which dislocations are able to move within the material. This will be further discussed in Chapter 2.2 [36].

### 2.1.3 Ductile fracture

Nucleation, growth and coalescence of microscopic voids that initiate at impurity atoms and second phase particles is the usual cause of ductile material failure. Pure materials with a very small volume fraction of inclusions may have a very large elongation to fracture, while high impurity metals (engineering material) fracture at a much lower strain, as illustrated in Figure 2.1.3. This is caused by void nucleation at inclusions. These voids then coalescence and a microcrack is formed, which lead to loss of load bearing capacity and fracture [6].

Usually the process of ductile fracture can be divided into three stages:

1. A free surface starts to form at a second-phase particle or inclusion by either interface decohesion or cracking of the particle.
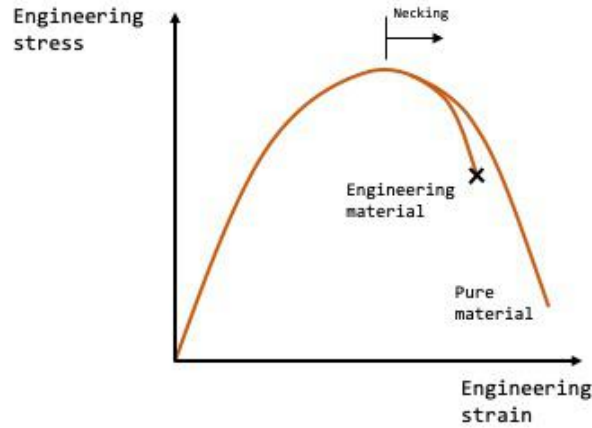
Figure 2.1.3: *Illustration of the difference in elongation to fracture for engineering materials with and pure materials. Based on figure from [6]*

2. The void grows around the particle as a consequence of plastic strain and hydrostatic stress.

3. The growing void coalescence with neighbouring voids.

For a void to form around a particle a sufficiently large stress is needed to break the interfacial bonds between the particle and the matrix. There exist numerously of models that estimate the void nucleation stress. The most commonly used model proposed by Argon et. al. [7] is based on that the interfacial stress at a cylindrical particle is approximately equal to the sum of the mean hydrostatic stress and the effective von Mises stress. The sum of these two stresses defines the decohesion stress. According to this model, the nucleation strain decreases as the hydrostatic stress increases. This means that void nucleation occurs more often in a triaxial tensile stress field, which according to Anderson [6] is a result that is consistent with experimental observations. Once voids have formed, they grow and coalescence as a result of further plastic strain and hydrostatic stress. The process is illustrated in Figure 2.1.4.

### 2.1.4 Modeling of Porous plasticity

When modeling porous metal plasticity the model is usually assumed to consist of a matrix material with a certain fraction of voids. In contrast to metals in general, which are assumed to be pressure-insensitive, porous metals are compressible. During straining both volumetric and deviatoric plastic strains develop. There is a competition between the matrix material which work-hardens and the voids which nucleate and grow and softens the material.

A popular model for describing porous metal plasticity is one that first was proposed by Gurson, [23], and later modified by Tvergaard, [53]. This model analyzes the plastic flow in a porous medium by assuming that the material is a continuum. The voids are taken into account by their influence on the global flow behavior. Since the material is assumed to be continuous and homogeneous the effect of the voids is averaged through the material. The yield criterion $g$ in this model is defined as, [6]:

$$g = \frac{\sigma_{eq}^2}{\sigma_M^2} + 2fq_1 cosh(\frac{q_2\sigma_{kk}}{2\sigma_M}) - 1 - q_3 f^2 = 0 \tag{2.1.5}$$

6
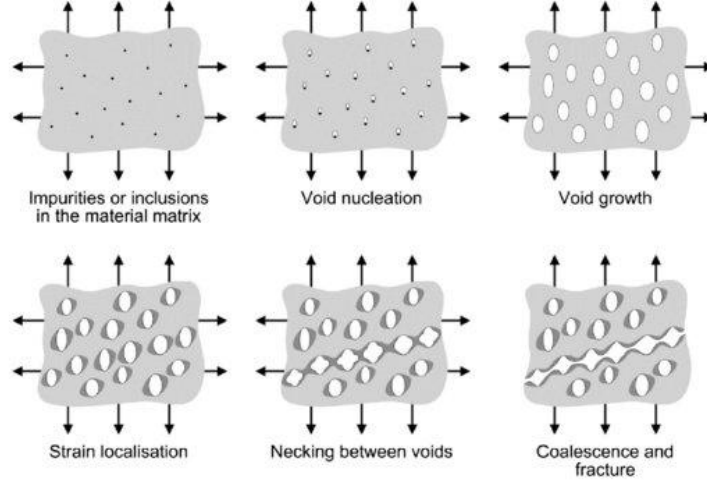
Figure 2.1.4: *Void nucleation, growth and coalescence in ductile materials (a) inclusions in a ductile matrix, (b) void nucleation, (c) void growth, (d) strain localization between voids, (e) necking between voids, (f) void coalescence and fracture [6].*

Where $q_1$, $q_2$ and $q_3$ are phenomenological fitting parameters and f is the current void volume fraction. $q_1$ modifies the void volume fraction and thus affects the yielding, $q_2$ is a correction factor for the hydrostatic stress, $\sigma_{kk}$ and $q_3 = q_1{}^2$. The three parameters together affect the form of the yield surface. Values of $q_1 = 1.5$, $q_2 = 1.0$ and $q_3 = q_1^2$ are typical for metals. With 0 void volume fraction ($f = 0$) the von Mises yield surface for an incompressible material is recovered. Further, $\sigma_M$ is the flow stress of the matrix material, $\sigma_{eq} = \sigma_{VM}$ is the equivalent von Mises stress and the hydrostatic stress is defined as $\sigma_{kk} = \sigma_{11} + \sigma_{22} + \sigma_{33} = 3\,\sigma_m$ where $\sigma_m$ is the mean stress and $\sigma_{11}, \sigma_{22}, \sigma_{33}$ are the normal stresses.

According to Anderson [6] voids grow very rapidly when the void fraction exceeds 10 to 20%. In equation (2.1.5) the rapid void growth and coalescence of the final stage is not sufficiently captured. Failure is hence often assumed when a critical void volume fraction $f = f_C$ is reached, where a typical value for carbon steels is $f_C = 0.15$. When the critical value is exceeded there is only a small amount of additional macroscopic strain before failure in real materials, which makes the assumption of failure at $f_C$ reasonable. Tvergaard - Needleman modified the original model by replacing $f$ with an effective void volume fraction $f^*$ which takes into account void nucleation and coalescence, in an attempt to capture the final stage before failure. This parameter is defined as:

$$f^* = \begin{cases} f & \text{if } f \leq f_C \\ f_C + \frac{\overline{f_F} - f_C}{f_F - f_C}(f - f_C) & \text{if } f_C \leq f \leq f_F \text{ where } \overline{f_F} = \frac{q_1 + \sqrt{q_1^2 - q_3}}{q_3} \\ \overline{f_F} & \text{if } \geq f_F \end{cases} \qquad (2.1.6)$$

where $f_C$ is the critical void volume fraction and $f_F$ is the void volume fraction at which there is a complete loss of load bearing capacity. According to Abaqus documentation [2], the above form of nucleation has shown accurate results for low triaxiality but is less exact for high triaxiality, with triaxiality defined as

$$\eta = \frac{\sigma_m}{\sigma_{eq}} = \frac{\sigma_1 + \sigma_2 + \sigma_3}{3\sigma_{eq}} \qquad (2.1.7)$$

7

Where $\sigma_e q$ is the von Mises stress and $\sigma_m$ is the mean stress, which affects the volume changes of the pores in the matrix [6].

## 2.2   Metallurgy

### 2.2.1   Crystal structure

Most metals are crystalline materials meaning that they have a periodic structure of unit cells, together forming the crystalline lattice (illustrated in Figure 2.2.1). The unit cell is the smallest repetitive structure that, in the case of a metallic crystal structure, by translation form the atomic or molecular structure.
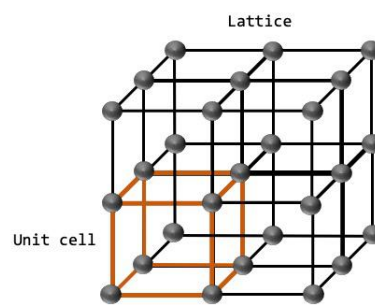


Figure 2.2.1: *A crystal lattice of periodic unit cells. Based on figure from [36]*

A total of seven crystal structures have been found in engineering materials, [15]. In metals three of them are the most common, namely the Body Centered Cubic (BCC), Face Centered Cubic (FCC) and Hexagonal Closed Packed (HCP). In the Figure 2.2.2, also the Body Centred Tetragonal (BCT) structure is presented. This is the structure of martensite.
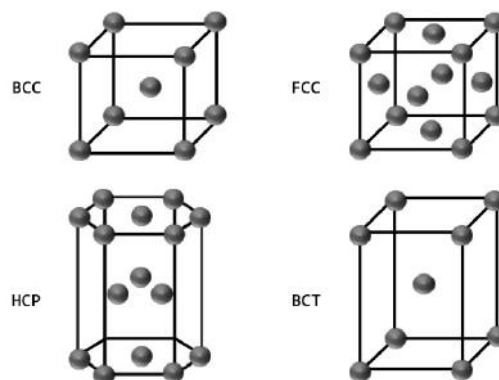


Figure 2.2.2: *The three most common crystal structures in metals and the crystal structure of martensite. Figure based on [36]*

The elastic behavior is only dependent on the crystal structure. The stretching of the bonds between the atoms is what governs the value of Young's modulus. Hence, the elastic stiffness is independent of microstructural factors such as grain size. Even alloying elements have little effect, as long as they don't change the crystal structure. However, the temperature affects the equilibrium separation of the atoms (increased separation at increased temperatures), which the modulus depends on. Consequently, Young's modulus tends to decrease with increasing

temperature [36].

## 2.2.2  Defects and strengthening mechanisms

How the material behaves in the plastic domain depends on both the crystal structure and defects in the structure. The mechanical properties of metals are strongly dependent on the defects in the material. A structure containing a defect has a lower state of total energy than a defect-free structure, thus all metals contain defects. The defects can be either point defects, line defects, planar/surface defects or volume defects [15].

**Point defects**

Point defects are vacancies, substitutional atoms, self-interstitial atoms and interstitial impurity atoms. Vacancies are voids where an atom is missing and substitutional atoms are atoms of a different kind than the the bulk material, that have taken the position of a host-atom in the lattice. These atoms are usually close in size to the host-atom. Interstitial impurity atoms take positions in between the host atoms, and are hence usually smaller in size compared to the host atoms. Carbon in steel is one example. Self-interstitial atoms are extra atoms of the bulk material.

Solid solution strengthening is a strengthening mechanism caused by point defects where dislocations interact with foreign atoms that are in solid solution. The strengthening mechanism is due to the associated strain fields that occur around both interstitial and substitutional solute atoms that are in mismatch with the host atoms. The mismatch is regarding differences in size and shear modulus.

Particle strengthening is yet another strengthening mechanism connected to point defects. When fine particles are dispersed in the lattice they act as obstacles and particle strengthening, or dispersion strengthening is obtained. Particle strengthening can occur as a consequence of two different mechanisms. The first one is due to the so called Orowan mechanism where the dislocations bow around obstacles, or more specific, incoherent particles. With coherent or semi-coherent particles the strengthening mechanism is instead due to shearing of the particles [15].

**Line defects**

Line defects are dislocations, areas in the lattice structure that are out of place in the crystal structure. When a stress is applied, dislocations are formed and moved and lead to slips, i.e. plastic deformation. There are two types of dislocations, edge dislocations and screw dislocations.

The edge dislocation can be seen as an extra half-plane in the lattice. The reason why the dislocation is called a line defect is because the locus of the defected points due to the dislocation lie along a line, a line running perpendicular to the extra half plane, illustrated as the dotted black line in the Figure 2.2.3. The dislocation allows for deformation to occur at a much lower stress than in a perfect crystal. This is because smaller parts can move at a time instead of moving the whole structure simultaneously. Only breaking a few bonds at a time require a much smaller force. The dislocation is slipping one plane at a time. Finally, the movement of the dislocation leads to a relative movement of the upper to lower part.
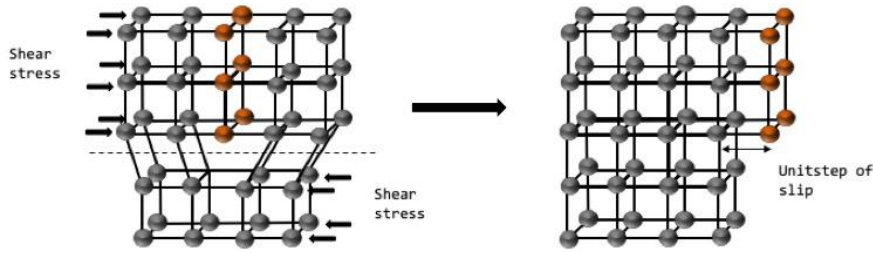
Figure 2.2.3: *Movement of an edge dislocation. Figure based on [15]*

The movement of screw dislocations is also a consequence of shear stress, see Figure 2.2.4. The direction of the dislocation motion is perpendicular to the stress direction, in contrast to for the edge dislocation. The process can be visualized as a block of metal being ripped by a shear force acting in different directions in the upper and lower part of the block. Also in this case, only a small portion of bonds have to be broken at a time, which require a smaller force than breaking all the bonds in the middle plane simultaneously. The stress required to move
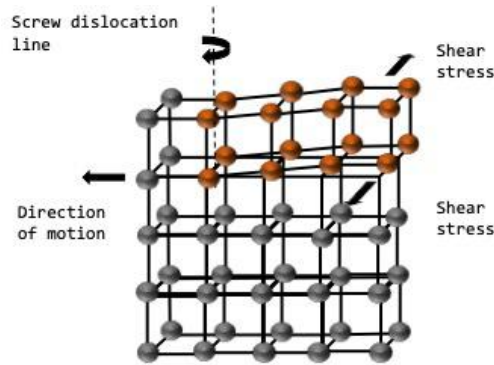


Figure 2.2.4: *Screw dislocation. Figure based on [15]*

the dislocation is called the Peierls-Nabarro stress. This stress is higher if the spacing between the atoms is large, hence dislocations move along the densest planes of atoms in the structure. FCC and BCC metals are dense and thus often ductile. In order to strengthen the metals, the movement of the dislocations have to be hindered, which can be done by obstacles like point defects, grain boundaries or by plastic deformation such that a large number of dislocations are formed and pin each other [36],[15].

**Planar defects**

Planar defects can be stacking faults, twin boundaries or grain boundaries. Stacking fault is when the sequence of the stacking of the planes is interrupted in one or two layers. If the stacking is not corrected immediately but continues a second stacking fault will form, which is a twin of the first one and a twin boundary is obtained. Grain boundaries acts as obstacles for the motion and length of the dislocations. At the grain boundary there is an increased disorder which causes discontinuity in the slip planes. With decreased grain size, the grain boundary area is increased, hence the material is strengthened. Grain size strengthening not only increases the strength, but also improves the toughness [36]. The size of the grain

boundary strengthening is given by the Hall-Petch relation:

$$\sigma_y = \sigma_0 + \frac{K}{\sqrt{d}} \tag{2.2.1}$$

where $\sigma_0$ represent the yield stress of the single crystal material, $K$ is a grain boundary strengthening factor that is material specific and $d$ is the grain diameter [15].

**Volume defects**

Volumetric defects act on a much larger scale than defects mentioned above, but they still affect the movement of the dislocations. Voids are example of volumetric defects and are defined as regions where a large number of atoms are missing. Another form of volumetric defect occurs when impurity atoms cluster together and form regions of another phase, which is called precipitates [15, 36].

---

## Literature review - Dual-phase steels

---

In this chapter a compilation of some of the previously conducted studies on DP steels is presented. The purpose of this review is to collect knowledge on what and how different parameters affect the mechanical behavior of DP steels. First a general description of the material is given as an introduction. Following sections discuss the influence of the governing parameters, while the two finishing sections present a variety of micromechanical models used for simulations of DP steels and studies of ductile fracture of the steel.

## 3.1 General

Dual-phase steel is a steel in the Advanced high strength steel (AHSS) family and has been developed since the 1970s. The microstructure of a ferritic phase with dispersed islands of martensite give the material its characteristic combination of properties, low initial yield stress, great ductility due to the soft ferrite, high ultimate tensile strength because of the hard martensite and a high initial strain hardening. These features make the steel an excellent choice of material in the automotive industry. Weight reduction of the car body, increasing passive safety systems and energy savings are benefits that the increased usage of DP steel has contributed to [17].

The microstructure of martensitic islands embedded in a matrix of ferrite, $\alpha$, is obtained from an intercritical heat method of an initial phase of ferrite and pearlite, as illustrated in Figure 3.1.2. The heating is followed by an accelerated cooling. When the temperature during heating reaches $A_1$ austenite, $\gamma$, appears. It is the austenite that later, during quenching, transforms to martensite, $\alpha'$, thus is the holding time above $A_1$ crucial for the final volume fraction of martensite [17]. By controlling the heating rate to the intercritical temperature, different martensite morphologies can be obtained. A higher heating rate lead to a banded microstructure where the grains are more elongated, while a lower tend to form primarily equiaxed microstructures with spherical grains [34].

Apart from martensite, bainite and retained austenite components may also exist. These phases are usually sought when improved edge stretch formability is desired [14].
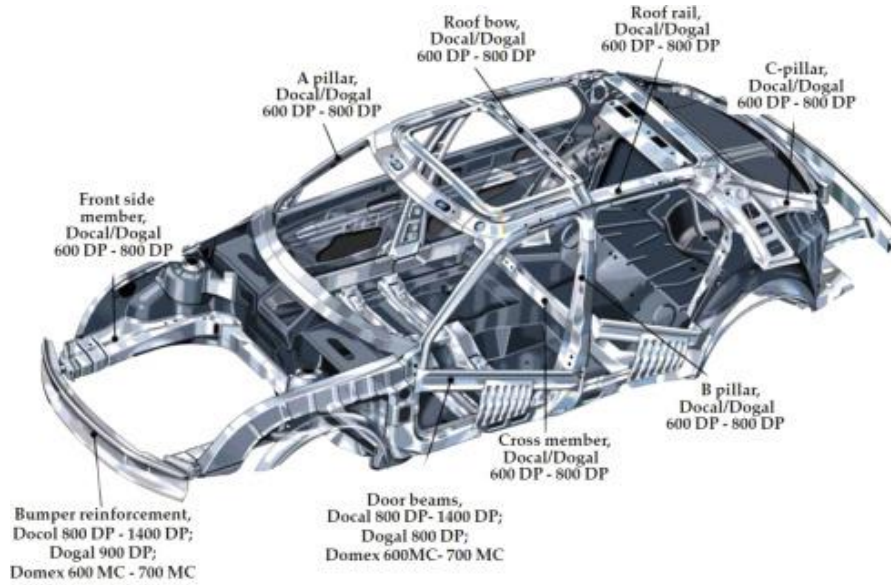
Figure 3.1.1: *Application of DP steels in cars, [21]*
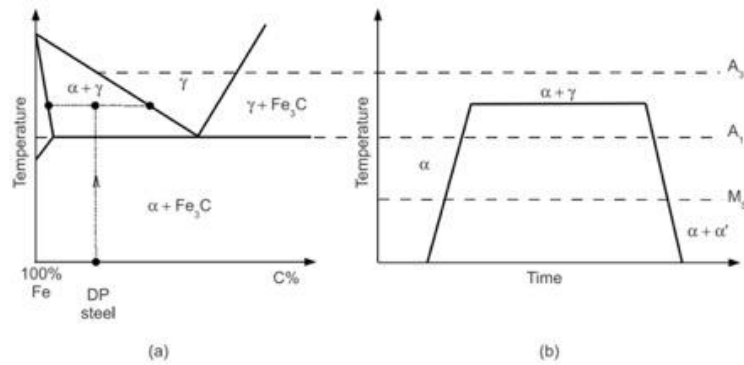


Figure 3.1.2: *Heat treatment when manufacturing DP steel: (a) schematic Fe-C diagram, (b) applied heat treatment, [32]*

## 3.2 Influence of alloying elements

To achieve the required microstructure additions of alloying elements are important. The carbon content is usually 0.06-0.15 wt% to give the martensite its strength. Manganese is added to solid solution strengthening ferrite. Both carbon and manganese also stabilize the austenite. To prevent the formation of pearlite and bainite, chromium and molybdenum are added and for promoting ferrite transformation silicon is added. Further, vanadium and niobium precipitation strengthen the material and refines the microstructure [14].

## 3.3 Influence of carbon

The carbon content in DP steels affects both the microstructure and the mechanical properties. According to Granbom [22], depending on the carbon content the martensite will appear in different morphologies. With a low to medium level of carbon content (up to 0.6 wt%) in the martensite a lath type of martensite is obtained. The type of lath also varies with the

14

carbon content, where a higher carbon content generates a more massive and dense appearance compared to martensite with a lower carbon content.

According to e.g. [19, 40] an increase in carbon content lead to increased 0.2% proof stress, ultimate tensile stress and hardness while the elongation to fracture decreases. The reason can, according to [40], be attributed to two different effects [40]. First, an increase in carbon content lead to a higher dislocation density, due to the fact that a higher carbon content in the austenite phase cause a higher volume expansion during the transformation from austenite to martensite. Secondly, the intrinsic properties of the martensite is affected by the carbon solid solution strengthening, which was described in Chapter 2.2.2.

## 3.4 Influence of grain refinement

Yield strength and tensile strength increases with grain refinement. That has been stated frequently in the literature, and the study by Calcagnotto et. al. [13] is one example. DP steels with approximately the same volume fraction of martensite and chemical composition, but with different grain sizes were studied. Conclusions made in the study were, except from that a decrease in grain size lead to increased yield strength and tensile strength, that uniform elongation and total elongation were hardly affected in their case since the plastic deformation of the martensite was negligible. However, the initial strain hardening rate increased. The increase in initial strain hardening rate is due to a higher number of dislocation sources, early interactions of the dislocations and the back stresses that are due to both martensite islands and ferrite grains smaller than 1 $\mu m^3$. Furthermore it was stated that an increase in yield strength and the strain hardening rate of the ferrite matrix due to grain refinement results in rapid stress transfer to martensite. The consequence being that the yield stress of the martensite is reached at lower strains than in microstructures with coarser grains.

Chang and Preban [16] studied the correlation between ferrite grain size and volume fraction martensite. They argue that the yield strength and tensile strength of DP steels are connected to the ferrite grain size through a Hall-Petch type dependence. Their conclusion was that the constant $K$ (in equation 2.2.1), increases with increasing volume fraction martensite, a conclusion drawn from an experimental data set. An explanation to this result was obtained by extending the dislocation pile-up model to DP steels in a similar manner as Petch did in his original paper, [39], deriving the Hall-Petch equation, but with two additional assumptions in this case. First, it is assumed that during yielding, plastic deformation is negligible and second, the probability of pile-up of dislocations at the ferrite/martensite interface or ferrite/ferrite interface is proportional to the volume fractions of respective phase.

## 3.5 Influence of volume fraction and distribution of phases

The transformation of austenite to martensite is associated with a volume expansion with strains being produced, as was mentioned in Section 3.3. These strains result in residual stresses in the ferrite surrounding the martensite islands which obviously increase with a higher volume fraction martensite. According to Calcagnotto et. al. [13] these internal residual stresses promote plastic flow, thus lowering the point of yielding. An additional consequence of the volume expansion is that plastic deformation is induced in neighbouring ferrite grains and a larger number of unpinned dislocations are produced, contributing to work hardening. If

concluding, a higher fraction of martensite is correlated to yielding of the steel at lower strains and the initial strain hardening is higher.

There is also a relation between the volume fraction of martensite and hardness. This was studied by Bères et. al. [9]. They studied three types of DP steels, also delivered by SSAB, and stated that there is a linear relationship between volume fraction of martensite and strength as well as hardness, with the constraint that the hardness tests have to be performed in the higher load ranges, from 0.05 to 1 kilopond (kp).

## 3.6   Influence of martensite morphology

As described in Chapter 3.1 different martensitic morphologies can be obtained depending on the processing history of the steel. Mazinani et. al. [34] studied how the morphology affected the plasticity of the martensite in DP steel. They investigated steels with both lath formed and equiaxed martensite. The load transfer in two phase materials is discussed. Since the elastic moduli is equal for the two phases there is no stress transfer to martensite in the elastic region. Hence the initial yielding of the martensite is dependent on the yielding of the ferrite. The form of the martensite affects the transition strain (i.e. the strain at which martensite starts to deform plastically) . With spherical elastic second phases Mazinani et. al. [34] found that, the transition strain is approximately 10 times the yield strain, which corresponding to 2 %. Further, it was found that the ratio of the particle stress to matrix stress was 2.5 and that this ratio was almost independent of the volume fraction of martensite. For the case of banded morphology of martensite, other values were found. The transition strain was greater, approximately 5 %. The ratio of particle stress to matrix stress was 3 to 3.6 and this ratio was to a small extent dependent on the volume fraction. This indicates that a banded microstructure favors martensite plasticity more than equiaxed martensite. Mazinani et. al. [34] further conclude that the morphology of the martensite has a greater impact at higher volume fractions of the phase.

## 3.7   Micromechanical modeling of Dual-phase steels

Micromechanical modeling involves numerical modeling of a limited volume of a material or a component. In recent times, micromechanical modeling gained popularity with several scientific researchers who investigate the mechanical properties of DP steels. With its distinguishable two phases, a DP steel may be reviewed as a heterogeneous material at the microscopic level. Numerous researchers have shown that micromechanical modeling using representative volume elements in the simulation of tensile tests is a well suited approach in studying plastic flow and damage in multiphase steels.

It is a common assumption in micromechanical models of DP steels that the particle size is uniform and evenly distributed. Al- Abbasi and Nemes [4] studied the effect of particle size differences by creating a micromechnical model of a unit cell with the martensite as spherical inclusions, of two different sizes, in a matrix of ferrite. They concluded that at a constant volume fraction of martensite, the particle size ratio 1/2 (with one particle being of double the size of the other) leads to the highest strength measures. Furthermore, they reported that at lower volume fractions of martensite the effect of particle size ratio decreases, the reason being that to obtain the ratio effect the martensite has to undergo plastic deformation, which only

happens in the larger particles.

Khaleel together with co-workers has in a series of paper e.g. [47, 48], used two-dimensional RVEs obtained from scanning electron microscope (SEM) to predict the macroscopic stress-strain response of DP steels. They used the model in simulations for predicting ductile failure as a consequence of plastic strain localization during the deformation process. Different boundary conditions were also tested. Later, microstructure modeling based on real microstructure has been used by many others [12, 13, 42, 51].

Even though a two dimensional RVE is, as proved by earlier mentioned researchers, able to predict flow stress based on continuum mechanical assumptions to an acceptable precision, three dimensional RVEs are unconditionally better at representing the reality. This is proved in the work by Ramazani et. al. [41] who introduced a three dimensional RVE constructed statistically with randomly distributed phases. When they compared the results between 2D and 3D-models it was obvious that the 2D prediction underestimated the response while the 3D modeling gave quantitatively reasonable predictions of the flow curve.

## 3.8 Damage of Dual-Phase steels

DP steels have been reported by numerous of researchers to fracture in a ductile manner where the three characteristic steps, nucleation, growth and coalescence of voids have been observed [27]. Void nucleation modes reported for DP steels are decohesion of ferrite-martensite interface, martensite cracking and debonding of ferrite grains where the two former are the most frequently occurring.

The progression of damage at different strain levels has been studied by both Butcher et. al. [11] and Toda et. al. [52]. They found that at lower strains voids mainly nucleate due to martensite cracking, whereas at higher strains the dominant mechanism is void nucleation by de-cohesion of ferrite-martensite interface. Further Butcher et. al. [11] report that the void nucleation rate with strain increase when approaching final failure. Henceforth voids are formed close to the crack tip, presumably due to that the triaxiality is enhanced in the vicinity of the crack tip.

It has been reported by Kim et. al. [29] that the initiation of voids in the DP steel depends on the morphology of the martensite. If the martensite distribution is coarse, the main fracture mechanism is ferrite cleavage while for finely distributed globular martensite the void initiation appears at the phase boundary. Krauss et. al. [30] uniquely observed all three earlier mentioned void formation mechanisms, while Gurland et. al. [49] report the void formation due to decohesion of the martensite-ferrite interface to be the only present mechanism.

Evident from this enumeration of ambigious results of origins of microvoids is that it can not be concluded that there only exist one mode of nucleation for DP steels. The variation in the results can be attributed to the differences in microstructual features such as martensitic volume fraction and carbon content in the martensitic phase. It can be concluded from the above mentioned reports that at high volume fraction martensite, void formation mainly occurs due to particle cracking and ferrite-martensite interface decohesion, while at lower volume fractions of martensite, no cracking of martensite is present.

Modeling framework

This chapter presents the micromechanical model used in this work and how it is established. The micromechanical model is, when herein described, divided into two parts, the axisymmetric model and the description of the plastic flow stress, referred to as the single phase material model. The first represents the geometry of the representative volume element (RVE) and the volume fraction of each phase. The latter establishes the constitutive behavior of each phase by defining the plastic flow where microstructural parameters are accounted for. The concept of periodic boundary conditions (PBC) and how the these are applied in the model is presented in an individual section, due to the importance of the boundary conditions when modeling the RVEs. The implementation of the model in Abaqus/CAE is presented in the final section.

## 4.1 The axisymmetric model

The model is constructed by a unit cell consisting of a solid sphere embedded in a cylinder, where the sphere represents the martensite and the cylinder the ferrite. The cylinders are axisymmetric cells and are approximations of hexagonal cylinders that are periodically stacked on the macroscopic scale, which is illustrated in Figure 4.1.1. The geometry of the axisymmetric model can be seen in Figure 4.1.2 where $s$ and $h$ is the radius of the cylinder and half of the total height of the cylinder respectively, $x_1$ is the coordinate axis in the horisontal direction and $x_2$ in the vertical direction, $r$ is the radius of the martensitic sphere and $E_1 - E_4$ are the four sides of the axisymmetric model. This model is based on the one used by Lai et. al. [31] and similar to the one used by Al-Abbasi and Nemes [4].
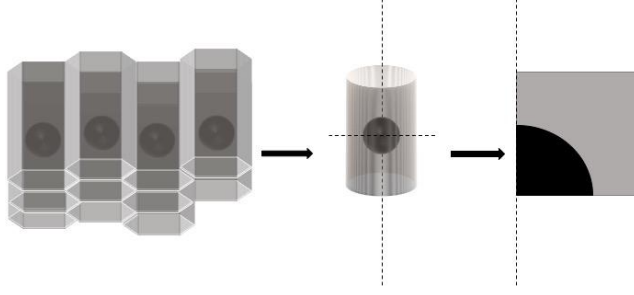
Figure 4.1.1: *From hexagonal stacked cylinders to the the axisymmeteric model. Based on figure from [31]*

This particular model has been reported by Al-Abbasi and Nemes [4] and Lai et. al. [31], to give successful results when simulating DP steel. The reason for the good results despite the simplicity of the model is believed to be due to the capability of the model to capture the main factors governing the behavior of the steel under uniaxial tension, namely the volume fraction of the two phases, the constitutive response of respective phase and how they interact. To obtain the desired volume fraction martensite, $V_m = V_{sphere}$, the radius, $r$ in Figure 4.1.2, of the martensite sphere is calculated as:

$$V_{sphere} = \frac{4\pi r^3}{3} \tag{4.1.1a}$$

$$V_{cylinder} = 2\pi s^2 h \tag{4.1.1b}$$

$$\frac{V_{sphere}}{V_{cylinder}} = \frac{2r^3}{3s^2 h} \tag{4.1.1c}$$

$$r = \left(\frac{3V_{sphere}s^2 h}{2}\right)^{1/3} \tag{4.1.1d}$$

Where $s$ and $h$ are defined in Figure 4.1.2 as the radius of the cylinder and half of the total height of the cylinder, respectively. These two measures are constant for all steels and are set to $s = h$ equal.

## 4.2 Periodic boundary condition

When a small and representative cell or element is used to approximate a large or even infinite system, periodic boundary conditions (PBC) should be chosen. The periodic boundary conditions create an infinite pseudo crystal of the unit cell and when a physical field, e.g. strain or stress is applied to the cell the PBCs copies the field from one side of the cell to the other side, such that the magnitude of the field reappears.

In order to simulate the macroscopic response of a unit cell subjected to tension, periodicity in the boundary conditions is crucial. This to maintain connectivity throughout the deformation process. In this case, with a cylinder as the unit cell, the outer surface has to be kept vertical, and for the axisymmetric model, to keep edge E3 in Figure 4.1.2 vertical. This is ensured by applying constraints. One way of describing the periodic constraints is given by Lai et. al. [31]:
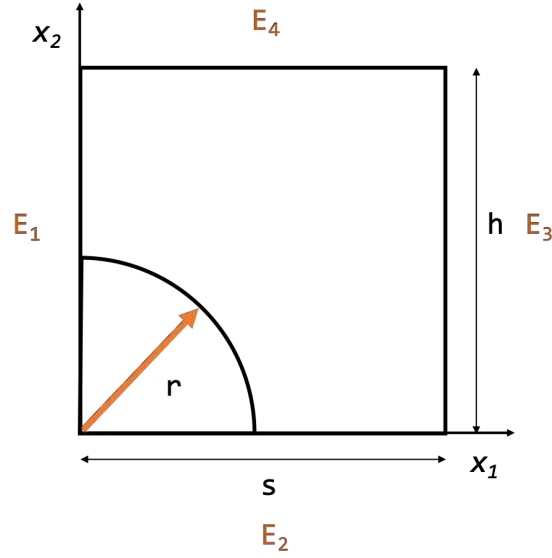
Figure 4.1.2: *Dimensions of the axisymmetric model. Based on figure from [31]*

$$u_2(x_1, x_2 = h) = \overline{u_2}, \quad 0 < x_1 < s \tag{4.2.1a}$$
$$u_2(x_1, z = 0) = 0, \quad 0 < x_1 < s \tag{4.2.1b}$$
$$u_1(x_1 = 0, x_2) = 0, \quad 0 < x_2 < h \tag{4.2.1c}$$
$$u_1(x_1 = s, x_2) = \overline{u_1}, \quad 0 < x_2 < h \tag{4.2.1d}$$

In condition 4.2.1a, a uniform displacement is applied, which corresponds to the macroscopic strain during the tensile test. The vertical displacement was set to $\overline{u_2} = 0.6h$ Displacement $\overline{u_1}$ in 4.2.1d is unknown, but also uniform in order to maintain periodicity. Condition 4.2.1b and 4.2.1c ensure symmetry with respect to the axis of symmetry E1 and the side E2.

## 4.3 The single phase material model

In the finite element analysis of the micromechanical model both ferrite and martensite need to be assigned an individual description of the flow stress. There exist two main methods to predict the flow stress of each single phase. The first approach is to create models based on empirical equations. The second method is employing physically based models which possess the advantage of linking both micro- and macroscopic scales.

In this work a physically based model proposed by Rodriguez and Guiterrez [44] and used by e.g. Ramazani et. al. [42] is used. The model and the resulting flow curves emerge from the dislocation based theory and the magnitude of strain hardening is based on dislocation density. The Hall-Petch grain boundary strengthening is added to the original model. The elastic modulus for both phases is assumed to be $E$=210 GPa and Poisson's ratio $\nu$=0.33. The flow stress consists of two parts, one strain independent friction stress and one strain dependent hardening stress as:

$$\sigma = \sigma_{friction} + \sigma_h = \sigma_0 + \Delta\sigma + \sigma_d + \sigma_h \tag{4.3.1}$$

Each individual contributing strengthening mechanism to the total flow stress (in MPa) is defined as follows (values of constants are summarized in Table 4.1):

- $\sigma_0$: the combined contribution from the Peierls stress and the strengthening from solute atoms

$$\sigma_0 = 77 + 750(\%P) + 60(\%Si) + 80(\%Cu) + 45(\%Ni) + 60(\%Cr) \\ + 80(\%Mn) + 11(\%Mo) + 50(\%N_{ss}) \tag{4.3.2}$$

- $\Delta\sigma$: the strengthening from $C$ in solid solution and precipitates

  For ferrite:
  $$\Delta\sigma = 5000(\%C_{ss}^f) \tag{4.3.3}$$

  For martensite:
  $$\Delta\sigma = P_1(\%C_{ss}^m) - P_2 \tag{4.3.4}$$

  $P_1$ and $P_2$ will be calibrated in Chapter 6.3.3.

- $\sigma_d$: Hall- Petch strengthening. Accounts for grain boundary strengthening.

$$\sigma_d = \frac{K}{\sqrt{d}} \tag{4.3.5}$$

  Where $d$ is the grain size and $K$ is the Hall-Petch constant.

- $\sigma_h$: the work hardening due to dislocation accumulation, originating from the Taylor equation, see derivation in the work by Hou [27].

$$\sigma_h = \alpha M \mu \sqrt{b} \sqrt{\frac{1 - exp(-Mk_r\varepsilon^p)}{k_r L}} \tag{4.3.6}$$

  Where $\varepsilon^p$ is the plastic strain, $M$ is the Taylor factor, $b$ is the magnitude of the Burgers vector, $\alpha$ is a constant, $k_r$ is a parameter controlling dynamic recovery and $L$ is the dislocation mean free path.

Table 4.1: Values of parameters in the single phase material model according to Rodriguez and Guiterrez,[44], * According Calcagnotto et. al. [12]. The subscripts $f$ and $m$ represent ferrite and marteniste respectively. Recall that $d$ refers to the grain size.

| $P_1$ [-] | $P_2$ [-] | $K_f$* [MPa d$^{1/2}$] | $K_m$ [MPa d$^{1/2}$] | $\alpha$ [-] | $M$ [-] | $\mu$ [GPa] | $b$ [m] | $k_{rf}$ [-] | $k_{rm}$ [-] | $L_f$ [m] | $L_m$ [m] |
|---|---|---|---|---|---|---|---|---|---|---|---|
| 3065 | 161 | 4 | 0 | 1/3 | 3 | 80 | $2.5 \times 10^{-10}$ | $10^{-5}/d_f$ | 41 | $d_f$ | $3.8 \times 10^{-8}$ |

From the parameters listed in Table 4.1 $P_1$, $P_2$, $k_r$ and $L$ are commonly used as fitting parameters. This is taken into accounted in the parametric study in Chapter 6.3.

## 4.4 Implementation

The axisymmetric model and the uniaxial tension test are simulated by the finite element method using the commerical finite element code Abaqus/CAE, version 6.14-4. Abaqus Implicit is used for the models simulating plastic deformation. The plastic flow stress of each phase is calculated separately with the Single-phase material model in a Python script. The material parameters are defined in a connected material card, one for each of the four steels. The calculated stresses and strains are implemented as user defined hardening in the Classical plasticity model in Abaqus. This model uses the von Mises yield surface and the associated flow rule.

The chosen elements are quadrangular with second-order interpolation function. For DP500, DP600 and DP800 reduced integration is used (CAX8R) while for DP980 full integration (CAX8) is needed to avoid distortion. The initial meshes have about 3000 elements. Mesh sensitivity is studied in Chapter 6.2.1. An example of inputfile for a model of DP600 is attached in Appendix B

A study of the method of implementing a ductile fracture criteria is done in Chapter 6.4, where the model had to be simulated in Abaqus Explicit. The possibility of the Classical plasticity model to be used in conjunction with damage and failure was utilized by adding the Porous Metal Plasticity model. This model uses the same elastic and hardening behavior as was defined earlier but the yield surface is changed to one based on the Gurson-Tvergaard-Needleman yield criterion, described in Chapter 2.1.4. The elements in this model are 4-noded bilinear with reduced integration (CAX4R).

Experimental procedures and results

The four DP steels, DP500, DP600, DP800 and DP980, delivered by SSAB were characterized and tested in microstructural- and mechanical properties. Microstructural and hardness properties data were supplied by PhD candidate Christian Oen Paulsen and results from tensile tests by Post Doctoral fellow Maria Jesus Perez. In subsequent sections the methods used, communicated from Paulsen and Perez, and the results from the tests are presented and post-processed. The three martensitic steels, 1200M, 1400M and 1700M, were also characterized and tested. Data from these tests can be found in Appendix A. It should be stressed that the experiments have not been conducted by the author, but by the mentioned suppliers of the data.

## 5.1 Microstructure characterization

The microstructure of the four DP steels are characterized by the use of Electron Backscatter Diffraction (EBSD). Three separate areas of 80 $\mu m \times 80 \mu m$ were studied for each steel. To identify martensite Image Quality (IQ) maps were used while the distribution and size of martensite islands were retrieved from studying binary versions of IQ maps. In Figure 5.1.1-5.1.4 the maps used for characterization are shown, a) IQ maps from EBSD, b) Binary version of IQ maps, c) Grain maps from EBSD of ferrite grains with martensite removed. For calculating linear size of martensite and free path of ferrite the following equations were used, [37]:

$$L_f = 2 \times \frac{V_f}{P_L} \tag{5.1.1a}$$

$$L_m = 2 \times \frac{V_m}{P_L} \tag{5.1.1b}$$

$P_L$ is the number of intersections per $\mu m$ on 80 horizontal lines and 80 vertical lines in the binary versions of IQ maps. For identifying ferrite grain size an area was first calculated by counting the number of points inside a grain. The diameter of the grain was then obtained by assuming the grain to be circular where the diameter of the circle represents the diameter of the grain. The microstructural data is given in Table 5.1.
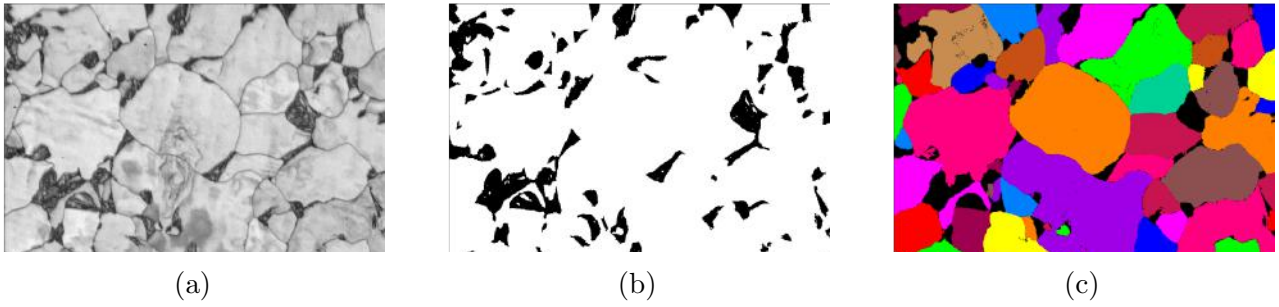
Figure 5.1.1: *DP500: a) IQ maps from EBSD, b) Binary version of IQ maps, c) Grain maps from EBSD of ferrite grains with martensite removed, [37]*
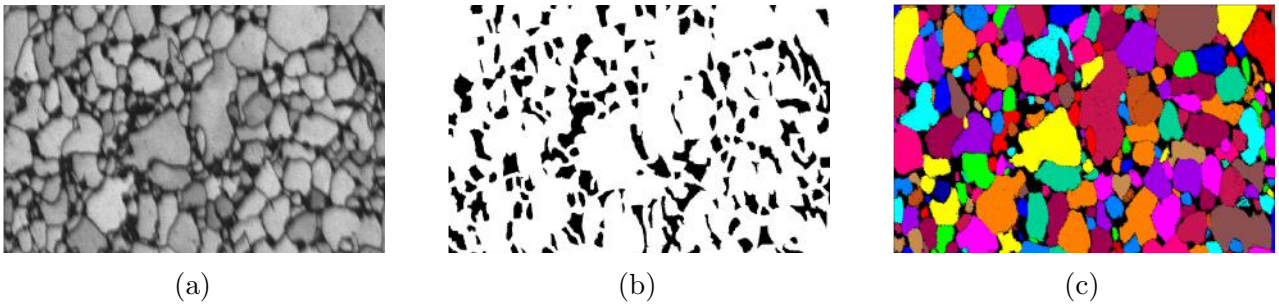


Figure 5.1.2: *DP600: a) IQ maps from EBSD, b) Binary version of IQ maps, c) Grain maps from EBSD of ferrite grains with martensite removed, [37]*
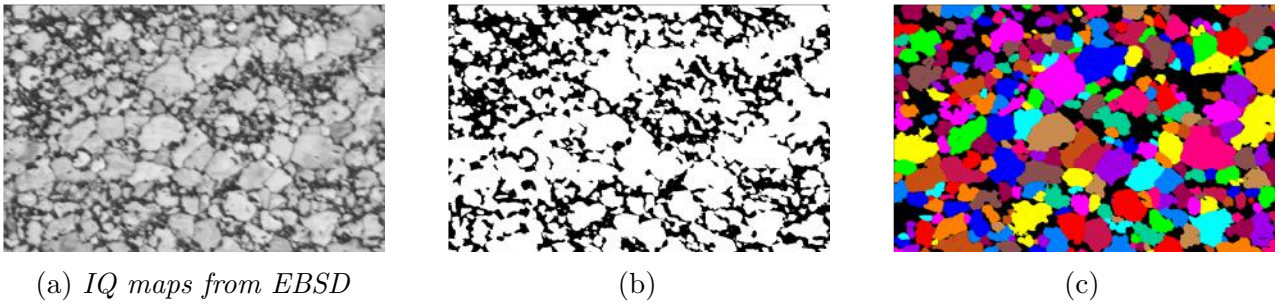


(a) *IQ maps from EBSD*

Figure 5.1.3: *DP800: a) IQ maps from EBSD, b) Binary version of IQ maps, c) Grain maps from EBSD of ferrite grains with martensite removed, [37]*
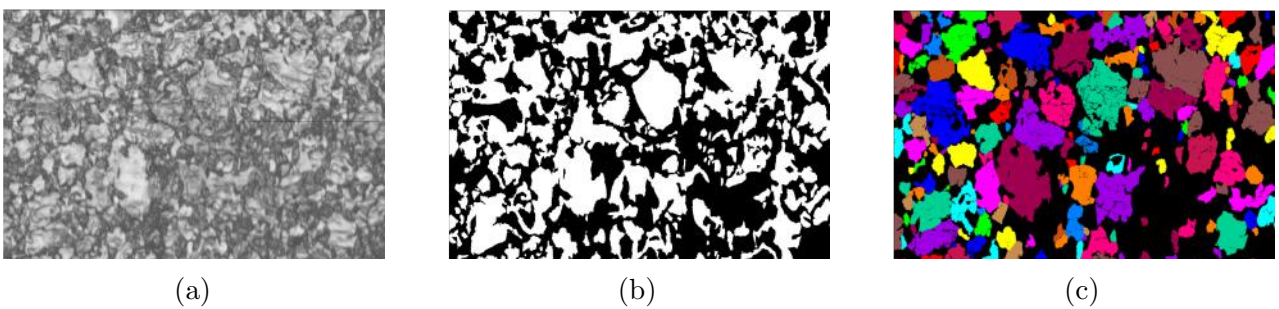


Figure 5.1.4: *DP980: a) IQ maps from EBSD, b) Binary version of IQ maps, c) Grain maps from EBSD of ferrite grains with martensite removed, [37]*

Table 5.1: Microstructure parameters, grain size= $d$, mean free path =$L$, volume fraction phase=$V$, [37]

|  | $d_m[\mu m]$ | $d_f[\mu m]$ | $L_m[\mu m]$ | $L_f[\mu m]$ | $V_m[\%]$ | $V_f[\%]$ |
|---|---|---|---|---|---|---|
| **DP500** | $3.41 \pm 2.74$ | $8.4 \pm 6.4$ | $2.5 \pm 0.4$ | $15.8 \pm 2.4$ | $14 \pm 0.3$ | $86 \pm 0.3$ |
| **DP600** | $2.27 \pm 1.26$ | $3.5 \pm 2.4$ | $1.5 \pm 0.1$ | $6.9 \pm 0.5$ | $18 \pm 2.2$ | $82 \pm 2.2$ |
| **DP800** | $1.94 \pm 2.15$ | $3.3 \pm 2$ | $1.5 \pm 0.2$ | $3.9 \pm 0.5$ | $28 \pm 3.2$ | $72 \pm 3.2$ |
| **DP980** | $2.47 \pm 8.45$ | $2.7 \pm 2.1$ | $7.8 \pm 0.7$ | $6.8 \pm 1$ | $54 \pm 1.3$ | $46 \pm 1.3$ |

As can be seen from Figure 5.1.1-5.1.4 and Table 5.1 the ferrite grain sizes are decreasing with increasing volume fraction of martensite. The martensite grain sizes are decreasing from DP500 to DP800, but with DP980 comes an increase. DP980 also has a much larger martensite volume fraction compared to the other three steel grades. The chemical composition was provided by the steel producer, SSAB, and is given in Table 5.2. Ferrite has a considerably lower carbon saturation point compared to martensite. It is therefore commonly assumed that the ferrite in DP steels is supersaturated in carbon, [13, 22]. At room temperature the ferritic carbon content is then, according to [14, 43], $C_f = 0.008$. It is further assumed that the rule of mixture is applicable:

$$C_{tot} = C_f V_f + C_m V_m \tag{5.1.2}$$

Such that the carbon content in the martensite may be computed as:

$$C_m = \frac{C_{tot} - C_f * V_f}{V_m} \tag{5.1.3}$$

Table 5.2: Chemical composition, [45]

|  | C | Nb | Mn | Si |
|---|---|---|---|---|
| **DP500** | 0.079 | 0 | 0.7 | 0.3 |
| **DP600** | 0.094 | 0.015 | 0.9 | 0.2 |
| **DP800** | 0.136 | 0.016 | 1.6 | 0.2 |
| **DP980** | 0.144 | 0.015 | 1.5 | 0.19 |

## 5.2 Mechanical properties

The mechanical tests conducted on the steels in order to obtain mechanical properties such as strength and ductility were tensile tests and Vickers Hardness tests. The tests were not only performed on the four DP steel but also the three pure martensitic steels. The results for the DP steels are given below.

## 5.2.1 Tensile test

Standard quasi-static tensile tests were performed according to the procedure described in Chapter 2.1.1 for all of the four DP steels. Four tests were performed for each steel. In Figure 5.2.1 the geometry of the specimens is given. The thickness was 1 mm for all of the steels except for DP500 which was 2 mm.

To obtain stress-strain curves from the test, DIC (Digital Image Correlation) was used. DIC is a method where digital photographs of the specimen at different stages of deformation are correlated. Some blocks of pixels are traced, from which surface displacement is measured. From this, it is possible to build up strain maps and deformation vector fields. For the method to work efficient it is important that the pixel blocks are unique and that there is a range of contrast, hence the specimens were painted in a black and white speckle pattern prior to the tests. A high frequency camera is used during the tests and the images taken are analysed in the DIC-software eCorr, see [20] for more information about the software. From the obtained force- displacement relation, engineering stress-strain and true stress-strain curve are calculated using equation 2.1.1 and 2.1.2. The resulting true stress-strain curve is given in Figure 5.2.2.

From the experimental data 0.2% proof stress ($\sigma_{0.2\%}$) and tensile stress ($\sigma_{TS}$) were identified and are presented in Table 5.3.
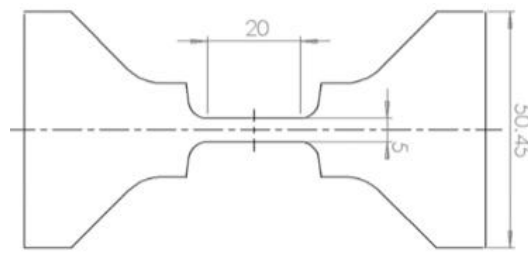


Figure 5.2.1: *Dimensions of specimen used in tensile test, [38]*
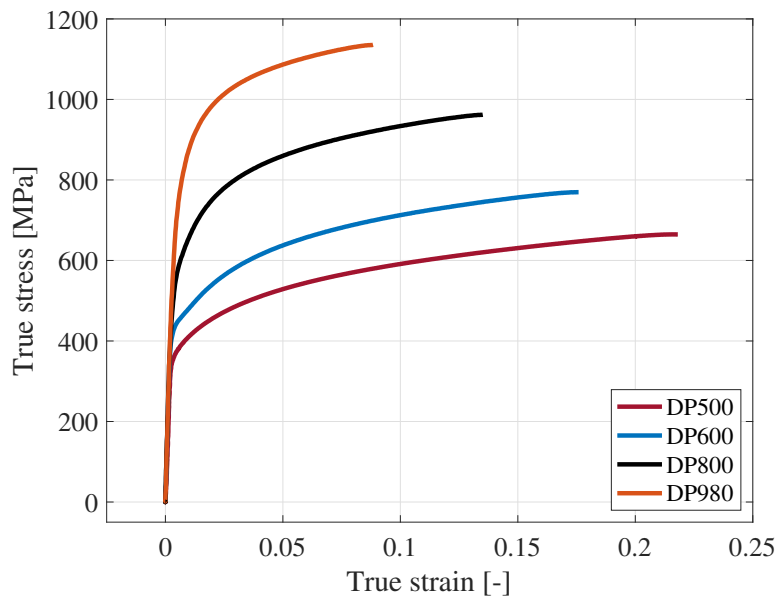


Figure 5.2.2: *Results from tensile tests, up to necking*

Table 5.3: 0.2% Proof stress and Tensile stress for each DP steel

|  | DP500 | DP600 | DP800 | DP980 |
|---|---|---|---|---|
| $\sigma_{0.2\%}$ [MPa] | 368 | 437 | 553 | 748 |
| $\sigma_{TS}$ [MPa] | 664 | 770 | 962 | 1136 |

### 5.2.2 Vickers Hardness test

In addition to the tensile tests, microhardness measurements were performed. Both the martensite phase and ferrite phase were measured in all acquired materials with an indentation load of 10 g (=0.01 kp) and a dwelling time of 15 seconds with seven repetitions. The equipment used was a Leica VMHT MOT, which produced the result given in Figure 5.2.3. In the figure, measurements on the steel both before and after heat treatment are presented. In this work only the measurements performed before heat treatment are used. In Chapter 5.3.1 the total hardness of the DP steel is required. Since the hardness measurements are only given for each phase separately, it is assumed that the total hardness of the steel can be approximated by the rule of mixture in the same approach as the carbon content in Equation 5.1.2:

$$H_{tot} = H_f V_f + H_m V_m \tag{5.2.1}$$
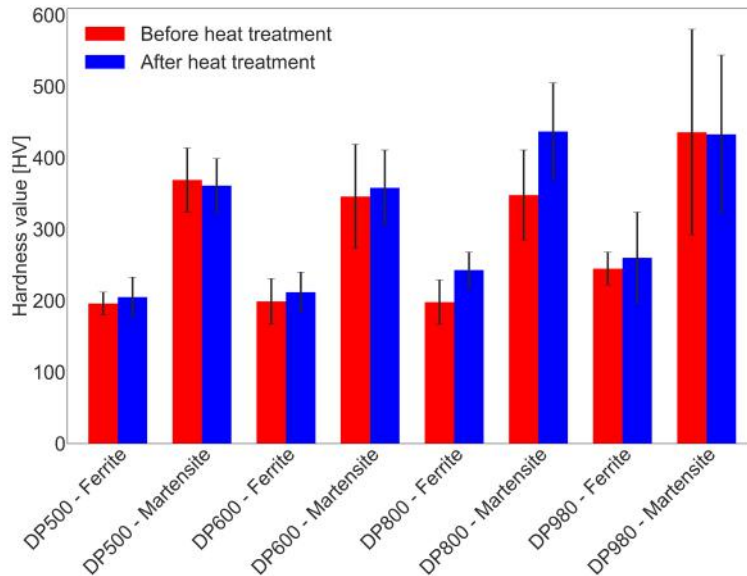


Figure 5.2.3: *Results from micro-hardness measurements, both before and after heat treatment. In this work only the measurements before the heat treatment are considered.* [37]

## 5.3  Post-processing of data

In this section the experimental data presented in previous sections is processed to find relations between microstructural and mechanical properties in order to gain more knowledge about the behavior of the material. This section is closely connected to the literature study in Chapter 3, comparing the results from previously conducted studies to the current steels. In Section 5.3.1 the effect of volume fraction martensite on the 0.2% proof stress, ultimate tensile stress and hardness is investigated. In Section 5.3.2 relations considering the carbon content are stated both for the DP steels and the martensitic steels.

### 5.3.1  Martensite volume fraction relations

The volume fraction of martensite is the primary factor affecting the properties of the material. It has been reported that both yield and ultimate tensile stress increase with increasing martensite volume fraction, [28, 40]. According to Figure 5.3.1 the same trend is present also in this case. For an ideal comparison, the carbon should have been kept constant with increasing volume fraction of martensite. However, as visualized in Figure 5.3.5, the carbon content in the martensite decreases with increasing volume fraction of martensite (this relation will be further discussed in Section 5.3.2). Subsequently the strength of the martensite phase is decreased with increasing volume fraction martensite, thus, a constant carbon content in the study would only strengthen the correlation found in Figure 5.3.1.

In addition, as discussed in Chapter 3.5 and reasoned by Pierman et. al. [40] the increase of the martensite phase in the DP steel also affects the ferrite phase due to the residual stresses induced from the austenite to martensite transition and the consequently increase in initial dislocation density. These dislocations are usually located at the interface between martensite and ferrite and hardens the softer phase. Also, as the martensite volume fraction increases a decrease in ferrite grain size, $d_f$, is induced and the Hall-Petch effect (see Equation 2.2.1) is increased. The volume fraction martensite is also compared to the total Vickers hardness approximated by the rule of mixture in Chapter 5.2.1. This is displayed in Figure 5.3.2. As was mentioned in Chapter 3.5, Béres et. al. [9] found a linear relationship between volume fraction martensite and hardness in their study. The best linear fit in the present work have a linear regression of $R^2$=0.962, shown in Figure 5.3.3. This value is not good enough for a linear correlation to be stated. However, Béres et. al. [9] further concluded that a linear relation only can be found if the hardness measurements are done with an indentation load of at least 0.1 kp. As mentioned in Chapter 5.2.2, the indentation load in this case was 0.01 kp. Hence, as is also stated in the suggestions of future work in Chapter 8, additional Vickers hardness measurements should be performed with higher indentation loads. It could then be expected to find a linear relationship.
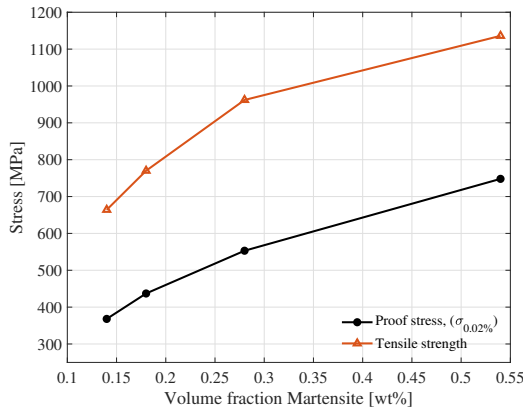
Figure 5.3.1: *DP steel: Stress (both $\sigma_{0.2\%}$ and $\sigma_{TS}$) versus volume fraction martensite.*
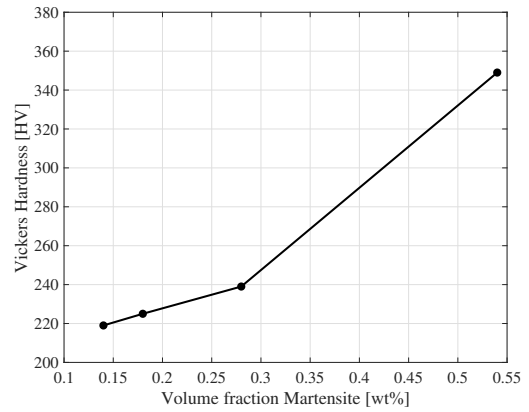


Figure 5.3.2: *The total Vickers hardness approximated by the rule of mixture versus volume fraction martensite*
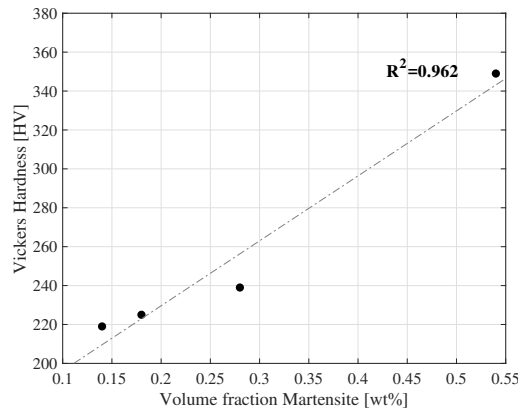


Figure 5.3.3: *Vickers hardness versus volume fraction martensite with a linear fit and the linear regression to this fit*

## 5.3.2 Carbon content relations

In the literature review on the influence of carbon content in Chapter 3.5 it was stated that an increase in carbon contributed to an increase in 0.2% proof stress, ultimate tensile stress and hardness.

In the four DP steels in this work both martensite volume fraction and carbon content in martensite vary for all steels, which makes it difficult to directly draw the same conclusions as in the literature. In Figure 5.3.6 the stress, both 0.2 % proof stress and ultimate tensile stress versus carbon content in martensite is shown, and in fact, the strength decreases with increasing carbon content in the martensite, contradicting the reported results from the literature.

In Figure 5.3.4 the total carbon content is increasing with increasing volume fraction martensite, nevertheless the carbon content in the martensite decreases with increasing volume fraction martensite. This is due to that the carbon content in ferrite is constantly supersaturated and do not change, so when the martensite volume fraction increases the carbon is diluted. Consequently the steel with the highest volume fraction martensite, DP980, has the martensite with the lowest strength. However, if once again referring to Figure 5.3.6, the effect of a large

volume fraction martensite has a larger impact on the strength than the carbon content.

With the results from the martensitic steels it is possible to study the martensite as a single phase, which is valuable since it is difficult to separate the ferrite from the martensite and the interaction between the two phases. In Figure 5.3.7 and 5.3.8 the sought correlation between carbon content and strength/hardness can be found. For both $\sigma_{0.2\%}$ and $\sigma_{TS}$ a linear relation exist and the same yield for the hardness. The linear relation between $\sigma_{TS}$ and carbon content will be used in Chapter 6.3.3 for calibration of the contribution from solid solution strengthening, $\Delta\sigma$, to the flow stress.
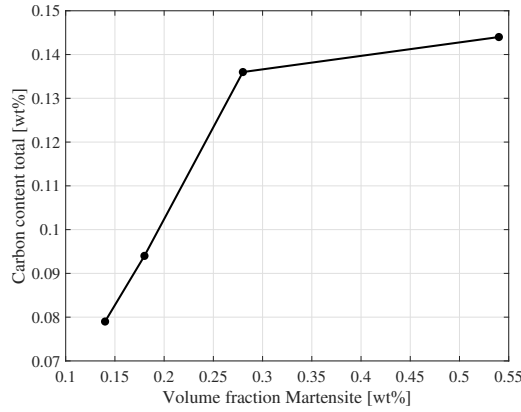
Figure 5.3.4: *DP steel: Total carbon content (both ferrite and martensite) versus volume fraction martensite*
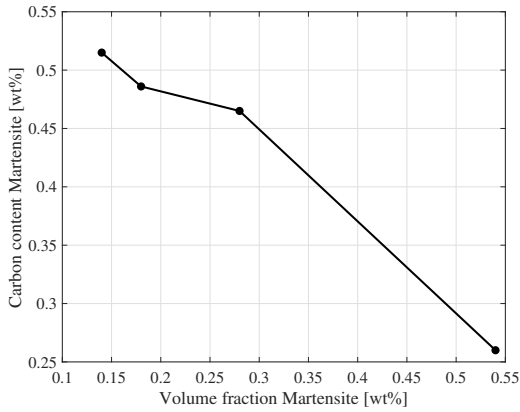


Figure 5.3.5: *DP steel: Carbon content in only martensite versus volume fraction martensite*
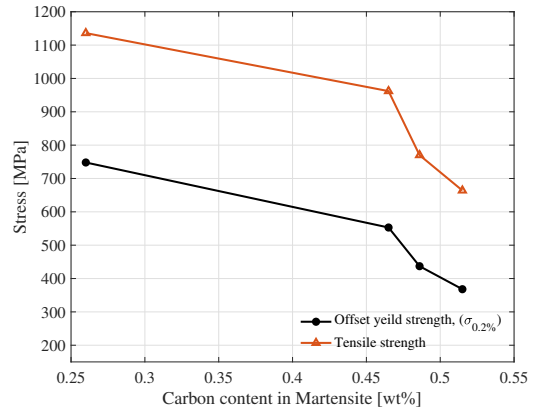


Figure 5.3.6: *DP steel: Stress (both $\sigma_{0.2\%}$ and $\sigma_{TS}$) versus carbon content in only martensite*
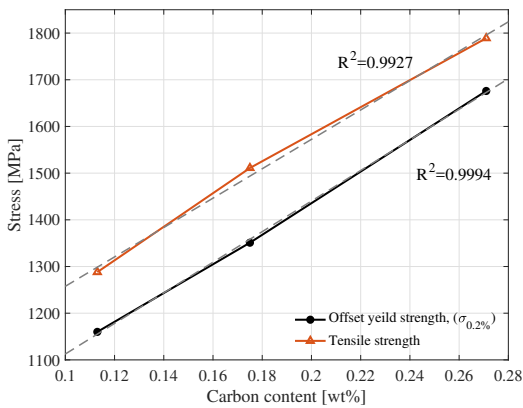


Figure 5.3.7: *Martensitic steel: Stress (both $\sigma_{0.2\%}$ and $\sigma_{TS}$) versus carbon content*
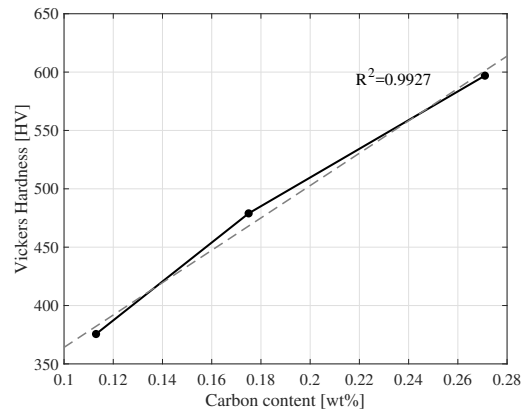


Figure 5.3.8: *Martensitic steel: Carbon content in martensite versus hardness*

Numerical Simulations

In this chapter results from the numerical simulations of the uniaxial tensile test is presented. Micromechanical simulations has been performed with the RVE presented in Chapter 4.1, implemented as an axisymmetric model in Abaqus. The utilized single phase material model described previously in Chapter 4.3 was applied to each phase in the model.

The analyses presented in the following text consist of two parts using the full described modeling framework: one where the axisymmetric model of the phase distributions is studied and another where the flow stress with the use of the single phase material model of the two individual phases is studied. The former documents importance of the geometrical representation of the two phases (and their interaction) while the constitutive descriptions of each phase are kept constant. In the latter part, the single phase material models are studied through parametric studies while the axisymmetric model representation is unaltered. Before these parts are presented, a base model is established and tested with constituent values corresponding to Rodriguez and Gutierrez [44].

In addition, a qualitative study of implementing and calibrating a Gurson - Tvergaard-Needleman damage model is given at the end of this chapter. The geometry of the base model is left unchanged and so are the microstructural parameters of the single phase material model. The yield criterion is changed from von Mises to the criterion described in Chapter 2.1.4.

## 6.1  Results - Base model

With the calculated plastic flow, from the single phase material model described in Chapter 4, implemented in the axisymmetric model described in the same chapter, predictions of the tensile test response were obtained. Contour plots of the plastic strain for each steel at nominal strains of 0.1, 0.2 and 0.3 are shown in Figure 6.1.1 where the limits of the color-bar are auto-computed for each frame. Figure 6.1.2 also visualizes the equivalent plastic strain at nominal strain of 0.2, but with the color-bar fixed and based on an interval that shows the plastic strain in the martensite of DP800. The response is similar for all four steels. Equivalent plastic strain initiate at the grain boundary between martensite and ferrite and a band of high strain is formed in a direction of 45°to the loading direction. This is to expect due to

composite theory. The harder phase is subjected to a higher load than the softer, while the softer has a higher magnitude of deformation. The stress-strain incompatibility between the two phases causes the shear band.

In Figure 6.1.3 the equivalent plastic strain along the diagonal in the ferrite, from the grain boundary to the upper right corner, is plotted versus the distance from origo along the r-axis, for DP500. As can be seen the strain is very localized at the grain boundary.

What can also be read from the contour plots is that in DP500 and DP600 no plastic deformation in the martensite occurs. The martensite in DP800 has just started to yield with small values of plastic strain in the center of the martensitic sphere, but with too small values for any deformation of the martensite to be visible. However, in DP980 the martensite is clearly deformed and the whole martensitic phase experiences plastic strain.

This gives indications that the volume fraction of martensite is related to the accumulation of plastic strain in the martensitic phase, which is consistent with the work by Al-Abbasi and Nemes [4]. Physically this is backed up by the correlation found in Figure 5.3.1, where the full material strength increases with volume fraction martensite.

A qualitative evaluation of the micromechanical model is done by comparing the experimental results to the numerical predictions from the model. True stress-strain curves are shown in 6.1.4. A very precise agreement with regard to strain hardening and ultimate tensile strength is obtained for DP500 and DP800. The prediction of DP600 is less precise but still acceptable while the response of DP980 is significantly over-predicted. As DP980 has the highest volume fraction of martensite among the four steels and experiences an extended plastic strain in the martensite it is reasoned that the prediction of the ferrite phase is good while the representation of the martensite phase needs adjustments.

The calculated plastic flow stress evolution according to Equation 4.3.1 for each phase and for all DP steel grades is shown in Figure 6.1.5. The plastic flow stress of the martensitic phase for DP980 is considerably lower than for the three lower steel grades. This is due to the carbon dilution effect found in Chapter 5.3.2. The strengthening effect from carbon in solid solution is the major strengthening mechanism contributing to the initial yield stress. Thus, the significantly lower volume fraction carbon in the martensite of DP980, lead to a comparatively lower initial yield stress. The strain hardening of martensite is equal for all steel grades, pertaining to the constant values in Equation 4.3.6 for martensite. The variation in flow curves of the ferritic phases is less pronounced.
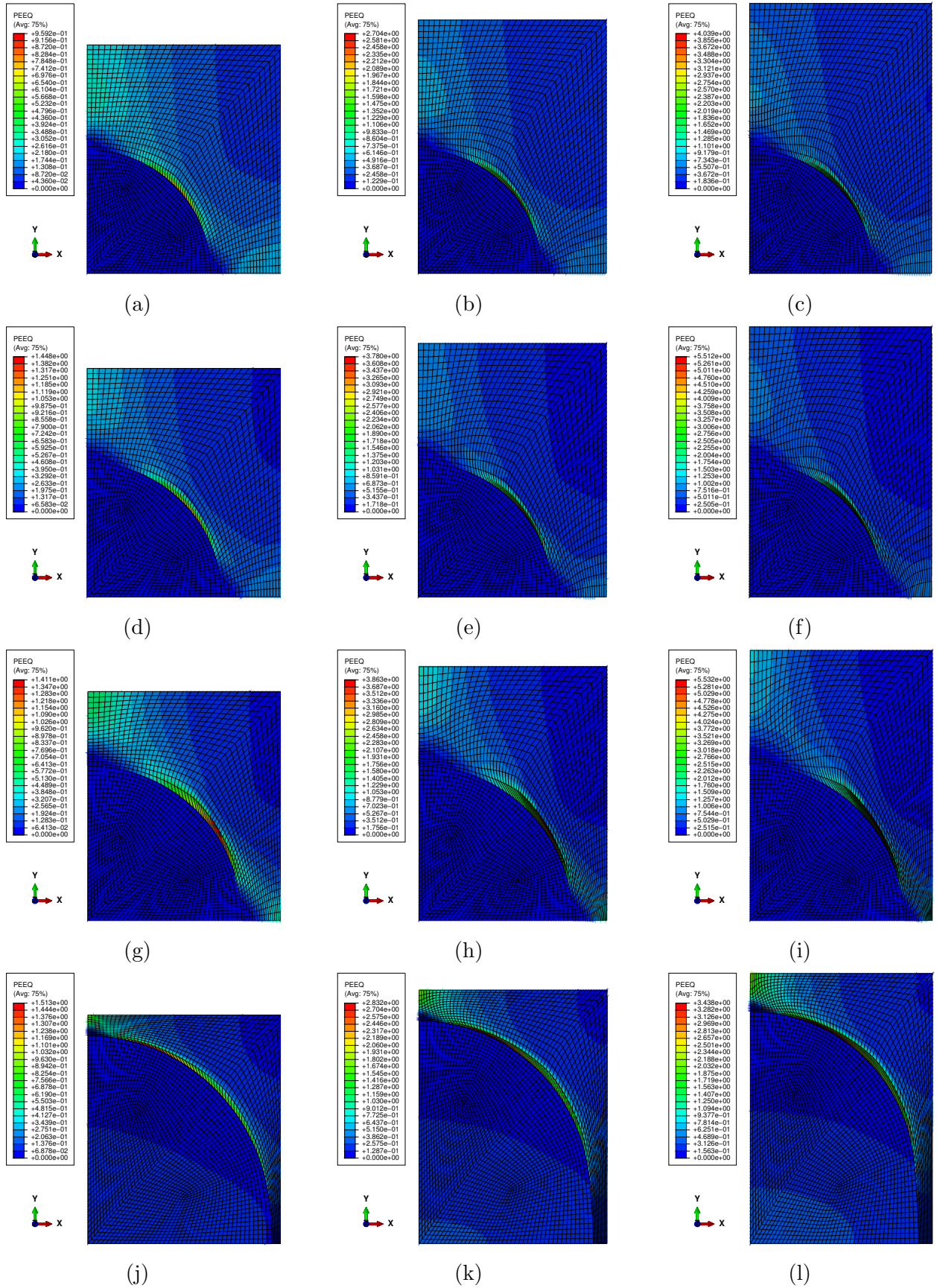
Figure 6.1.1: *Equivalent plastic strain (PEEQ) a)-c) DP500, d)-f) DP600, g)-i) DP800, j)-l) DP980 at nominal strains 0.1, 0.2 and 0.3. Limits of color-bar is auto-computed for each single figure*
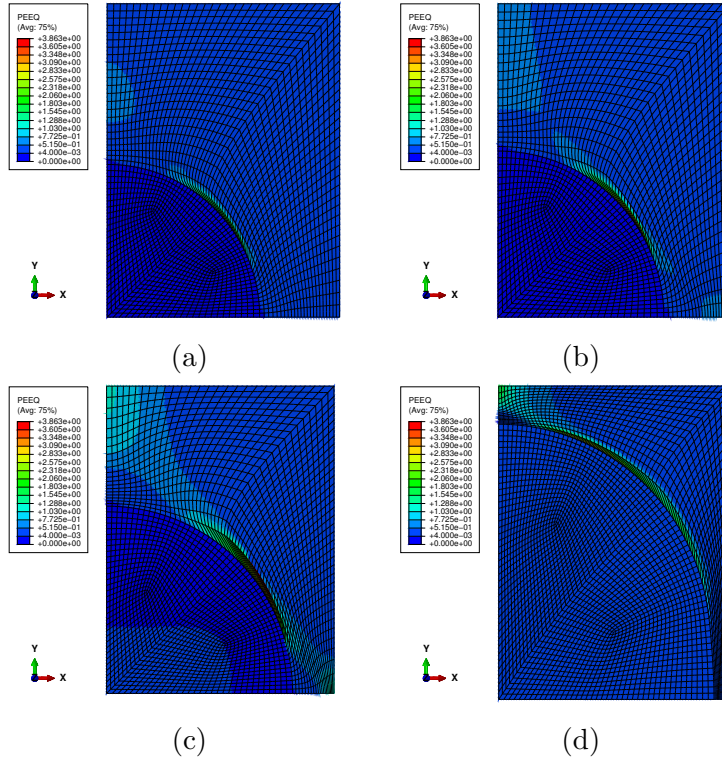
Figure 6.1.2: *Equivalent plastic strain (PEEQ) a) DP500 b) DP600 c) DP800 and d) DP980 at nominal strain 0.2 and with a fixed interval of the colorbar, based on a scale where the plastic deformation in the martensite of DP800 is shown.*
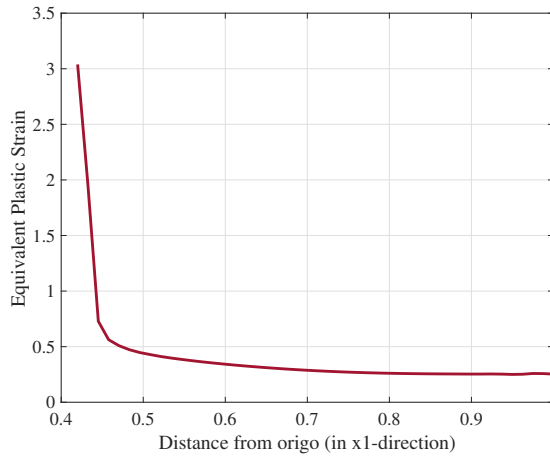


Figure 6.1.3: *Equivalent plastic strain along diagonal in ferrite, DP500.*

## 6.2 Evaluation and validation of Axisymmetric model

The results in the previous section show that the axisymmetric model, despite its simplicity, is able to simulate the uniaxial tension test of the steels with fairly satisfying results. In this section the model will be modified with the intention to evaluate and validate its response. The martensite particle size difference and the morphology of the martensite are studied.
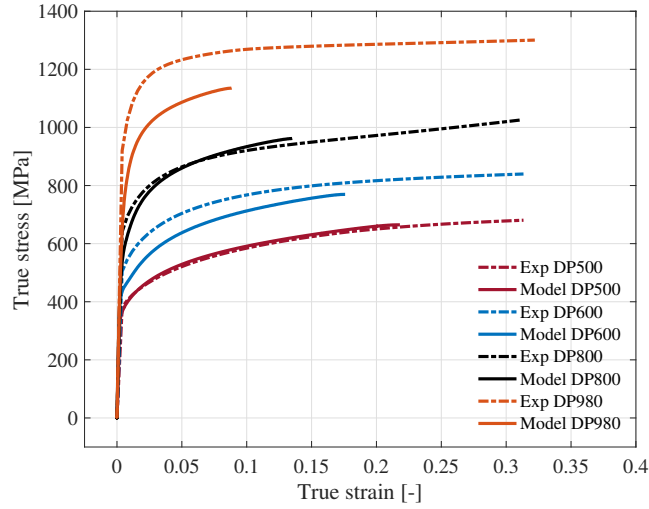
Figure 6.1.4: *Micromechanical predictions compared to experimental results with regard to true stress-strain curves. Input parameters according to Table 4.1*
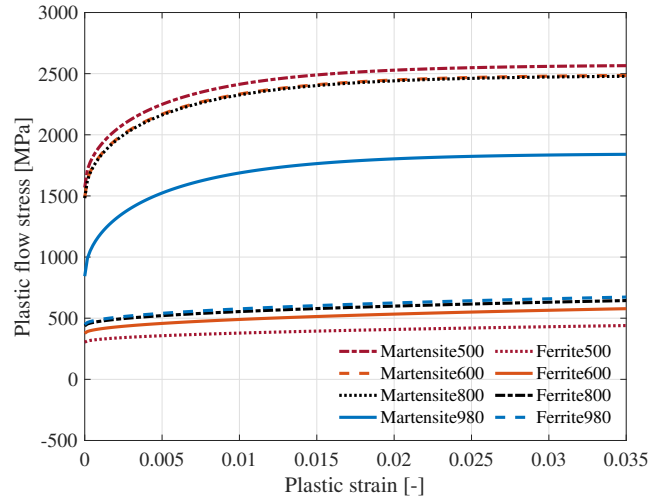


Figure 6.1.5: *Plastic flow curve for single phases. Input parameters according to Table 4.1*

### 6.2.1 Mesh-sensitivity

To examine if the mesh size has an effect on the result, the number of elements in the base model was both increased and decreased to those given in Table 6.1. The response from the study is shown Figure 6.2.1.

Table 6.1: Number of elements in mesh sensitivity study

|          | Min | Mean | Max  |
|----------|-----|------|------|
| **DP500** | 672 | 2526 | 5616 |
| **DP600** | 562 | 2218 | 5904 |
| **DP800** | 880 | 2714 | 5596 |
| **DP980** | 691 | 3455 | 5351 |

The number of elements has a negligibly effect on DP500, DP600 and DP980, with DP800 as an exception, which is assumed to be related to that the martensitic phase being in early stage plastification. Thus small changes in the model significantly impacts the stress response of the martensite. This was further studied by testing additional mesh sizes for DP800. For each mesh, the average equivalent plastic strain for a selection of elements in the center of the martensitic sphere was extracted. Number of elements in the mesh versus equivalent plastic strain is shown in Figure 6.2.2. There is an immense improvement going from around 1000 elements to 2000 elements but convergence is not obtained until about 8000 elements. However, as can be seen in Figure 6.2.3, the true stress-strain response is barely affected by changes in mesh size as the number of elements exceeds 2500. Therefore, it was decided to continue with the mean value.
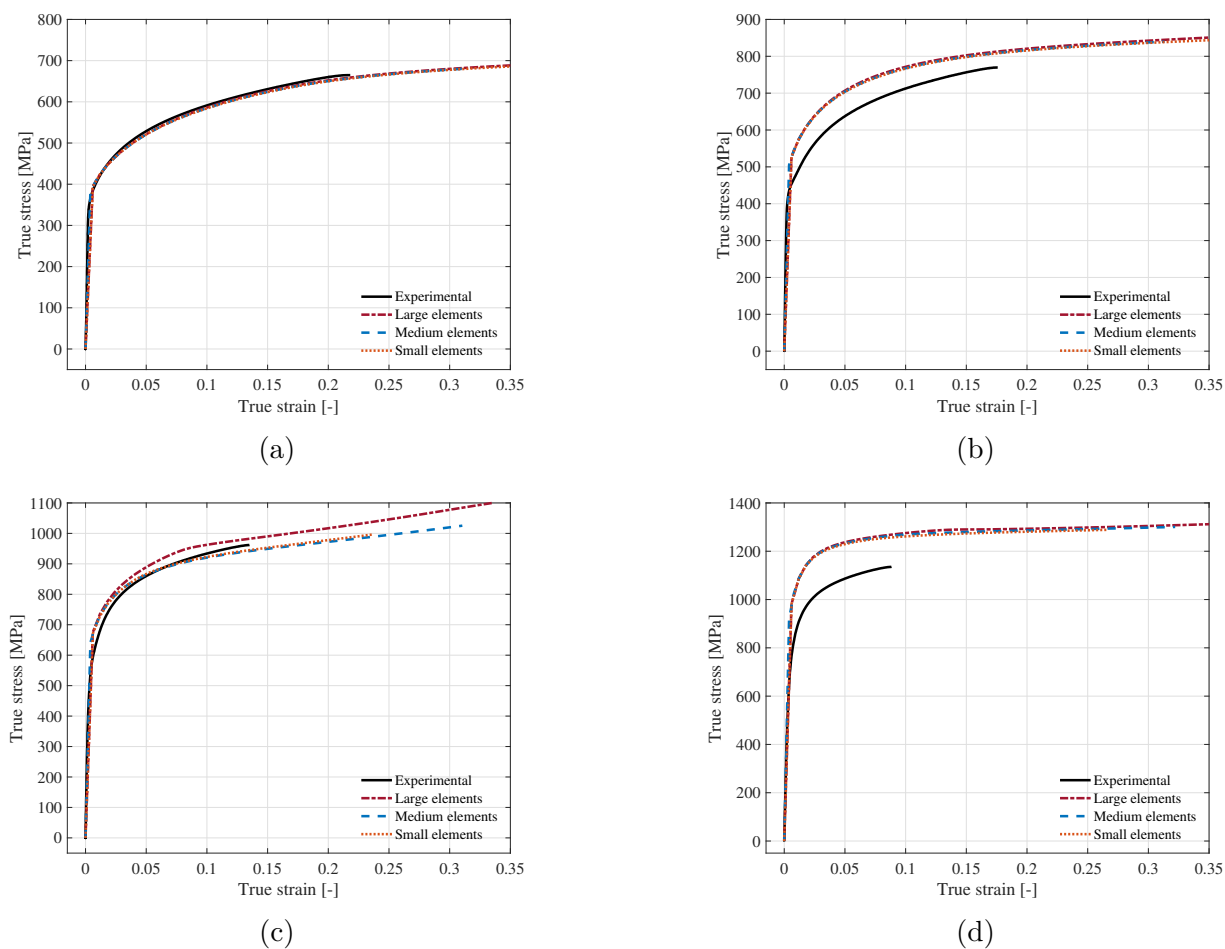


Figure 6.2.1: *Sensitivity study of mesh size for a) DP500, b) DP600, c) DP800 and d) DP980*

## 6.2.2 Double-model

As can be seen from the characterization of the steels, Table 5.1, there is a substantial spread in grain sizes, which means that there is a mix of larger and smaller grains. In order to investigate if the particle size difference has an effect on the response a similar model to the one analysed by Al-Abbasi and Nemes [4], mentioned in 3.7 is tested.
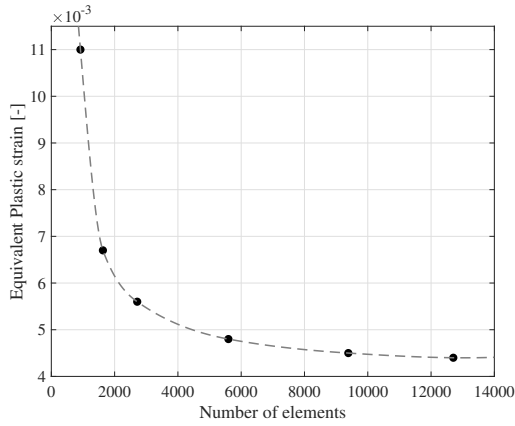
Figure 6.2.2: *Mesh size versus Equivalent plastic strain for DP800*
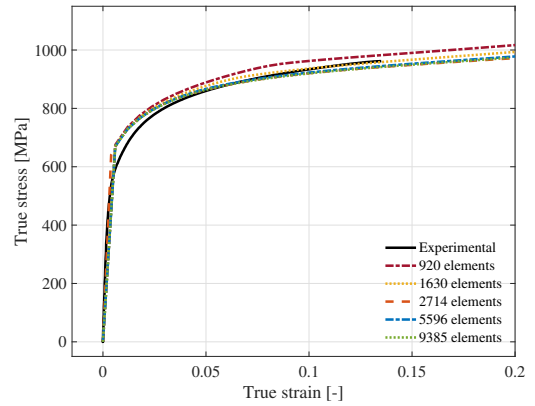


Figure 6.2.3: *Extensive sensitivity study of mesh size for DP800*

Modifications are made to the initial axisymmetric model so that the martensitic phase is represented by two islands as opposed to one (with the martensite volume fraction kept constant). This model will be referred to as the double-model, while the base model in this section is referred to as the single-model. The two phase radii, $a$ and $b$ defined in Figure 6.2.5, are calculated according to the equation below, where $x = a/b$:
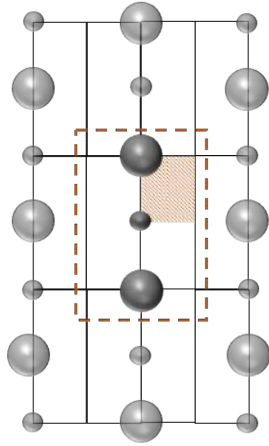


Figure 6.2.4: *The Axisymmetric RVE idealization of the double-model*
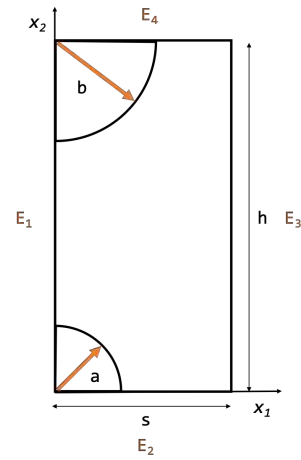


Figure 6.2.5: *Dimensions of the axisymmetric double-model*

$$Vm = \frac{2(a^3 + b^3)}{3s^2h} \tag{6.2.1a}$$

$$b = \left(\frac{3}{2}V_m s^2 h \frac{1}{x^3 + 1}\right)^{1/3} \tag{6.2.1b}$$

41
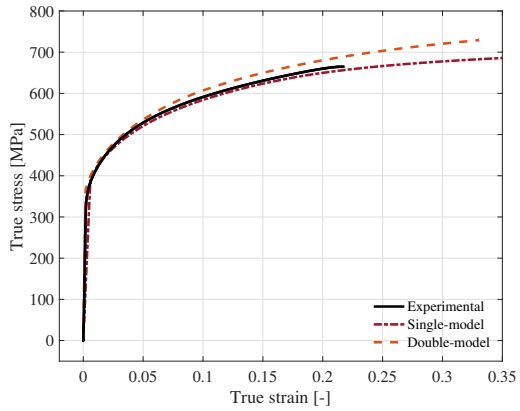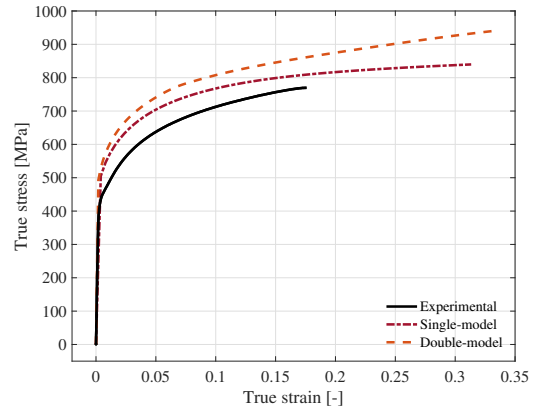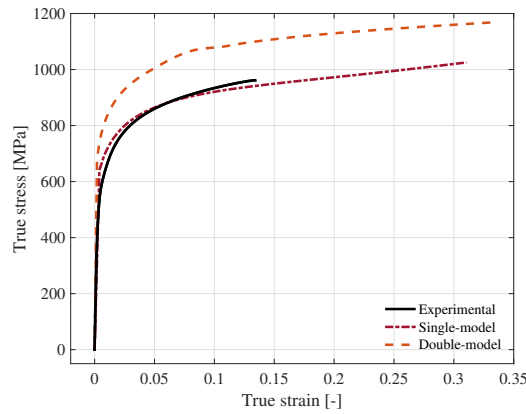
Figure 6.2.6: *True stress-strain curves, comparison between experimental results, single-model predictions and double-model predictions with x=1/2 for a) DP500, b) DP600 and c) DP800*
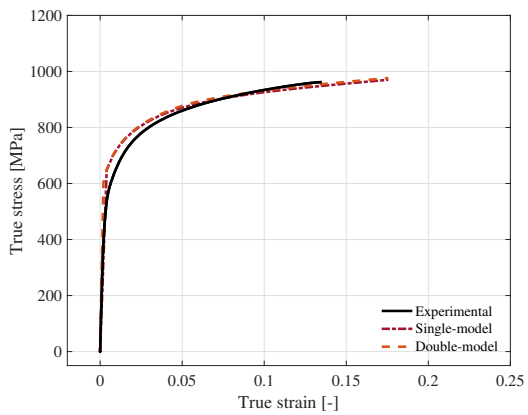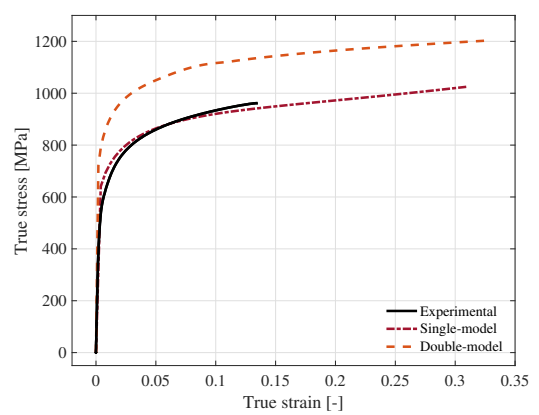


Figure 6.2.7: *True stress-strain curves, comparison between experimental results, single-model predictions and double-model predictions for a) x=1 b) x=1/16, both for DP800.*
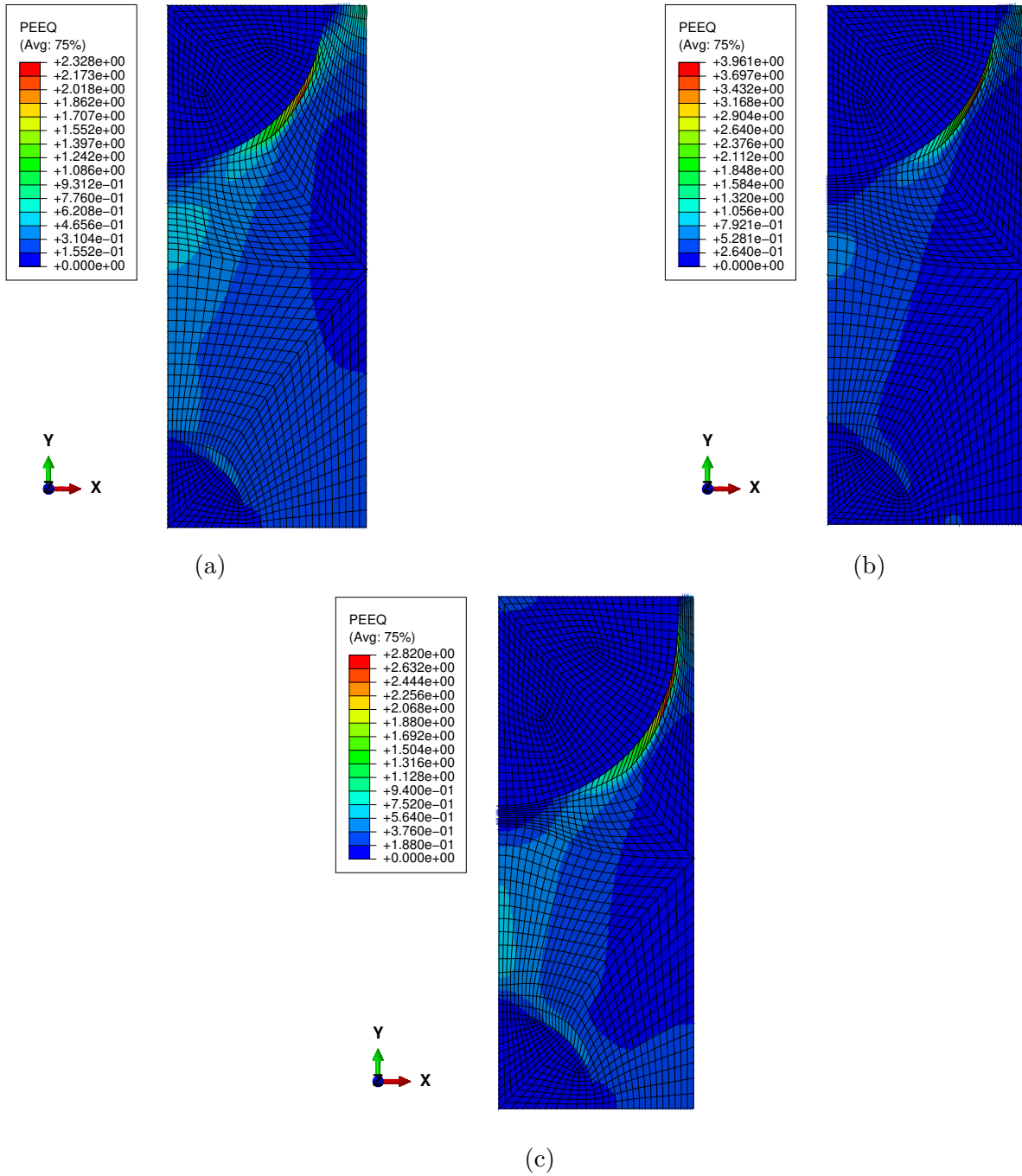
Figure 6.2.8: *Contour plot of equivalent plastic strain at nominal strain 0.2 with x=1/2 for a) DP500 b) DP600 b) DP800.*

In contrast to the single-model, $H$ and $L$ are not equal, a factor two is used instead such that $2L = H$. The boundary conditions are the same as stated in Equation 4.2.1 and used for the single-model.

For DP980 the radius of the sphere is almost equal to the radius of the cylinder ($b \approx s$) already with a ratio $x = 1/1$. Hence only DP500, DP600 and DP800 are included in the test. According to Al-Abbasi and Nemes [3] the largest particle size effect is obtained for the ratio $x = 1/2$, hence this is the ratio that is applied to all three steels. DP800 is further tested with $x = 1/16$ and $x = 1/1$ in order to investigate if an even larger particle leads to earlier yielding and to validate that it is not only the changed dimensions of the cylinder that have affected the response. In Figure 6.2.6 and 6.2.7 the numerical predictions of stress-strain response are compared to experimental results and the single-model predictions. Contour plots of equivalent plastic strain are given in Figure 6.2.8 and 6.2.9. There is a pronounced strengthening effect from particle size distribution. This effect increases with increasing volume fraction martensite. The strengthening effect is rather large, compared to the results reported by Al-Abbasi and Nemes. In addition, the model with $x = 1/16$ predicts higher strength than $x = 1/2$ (compare Figure 6.2.6c and 6.2.7b), which is contradicting the result reported by Al-Abbasi and Nemes. The prediction of the response with $x = 1/1$ is identical to the single-model prediction, as expected. The same is shown in the contour plots of the equivalent plastic strain where Figure 6.2.9b and the lower half in Figure 6.2.9a are identical.
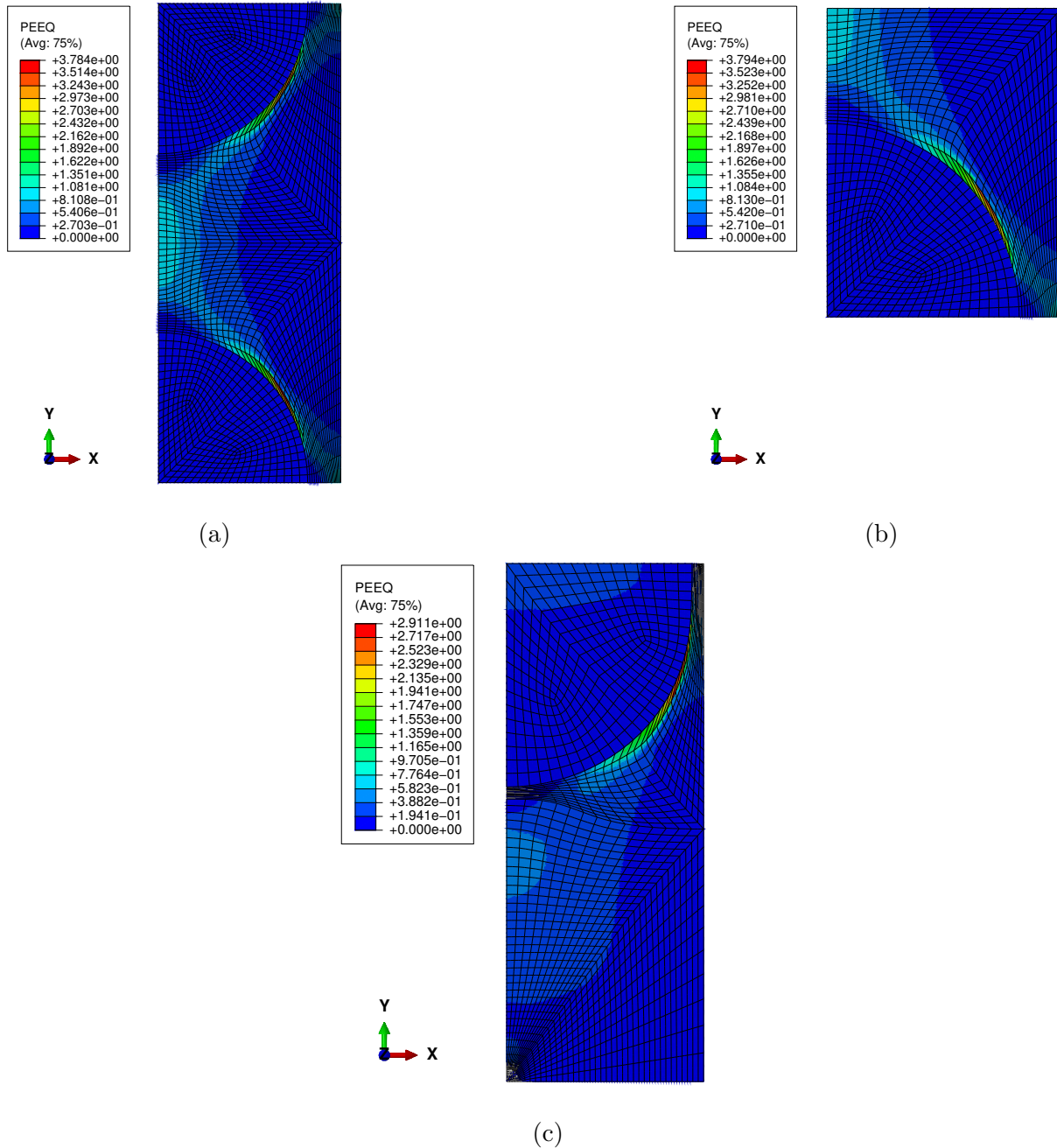
Figure 6.2.9: *Contour plot of equivalent plastic strain (PEEQ) at a nominal strain 0.2 for a)*
*Double-model, x=1/1 b) Single-model, c) Double-model, x=1/16.*

### 6.2.3  Ellipsoid-model

In Chapter 3.6 different morphologies of martensite were discussed, in particular how they affect the plastic deformation of martensite. So far, the martensite has only been represented as a perfectly round sphere in the numerical simulations, which is a satisfying approximation of the so called equiaxed formation of martensite. However, for the elongated grains, an ellipsoid formed martensite particle in the RVE is tested. According to Mazinani et. al. [34] a banded structure favors plastic deformation in the harder second phase. To study the influence of shape change a model with the geometry as in Figure 6.2.10 was implemented. With the same motivation as in Chapter 6.2.2, DP800 is the steel that the ellipsoid model will be applied to. The two shape parameters of the ellipsoid, a and b, are calculated according to Equation 6.2.2, where $x = a/b$.
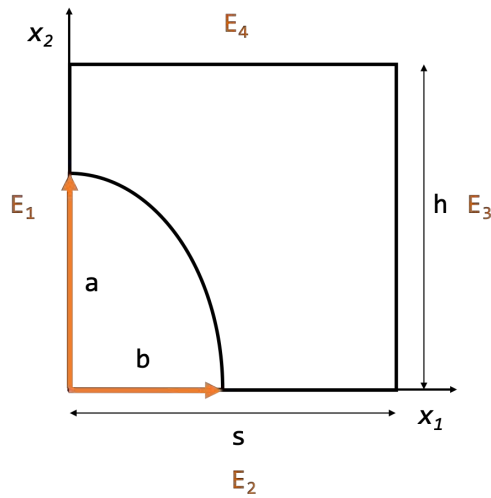


Figure 6.2.10: *Dimensions of the axisymmetric ellipsoid model*

$$V_m = \frac{4ab^2}{3s^2h} \tag{6.2.2a}$$

$$b = \left(\frac{3V_m s^2 h}{4x}\right)^{1/3} \tag{6.2.2b}$$

Two cases are tested, first with $a = 1.3b$ and then $b = 1.3a$. This model is referred to as the ellipsoid-model and the base model is here comparably cited as the sphere-model. The stress-strain response is compared to predictions from the sphere-model and the experimental results and can be found in Figure 6.2.11. In Figure 6.2.12 contour plots of the equivalent plastic strain at a nominal strain of 0.2 are shown. According to these results, the statement that elongated formations of the harder phase lead to plastic deformation at an earlier state is true. In both cases the total strength of the material increases when the martensite is not perfectly round, but to a considerably larger extent when the particle is elongated in a direction perpendicular to the loading direction. Both the highest value of plastic strain and the largest extent of yielding in martensite can be found in the model with $b = 1.3a$. It should also be noted that the ferrite is more compressed for this case due to the combination of elongation of grain in the $x_1$ and the loading direction in the $x_2$-direction.
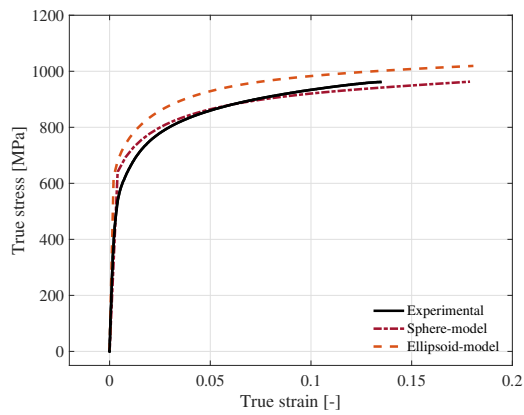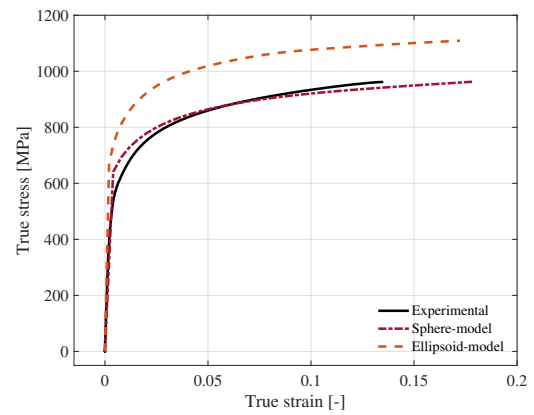
Figure 6.2.11: *Stress-strain prediction of the ellipsoid model with: a) a = 1.3b and b) b = 1.3a*
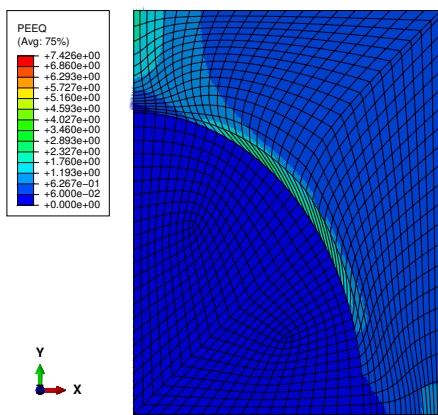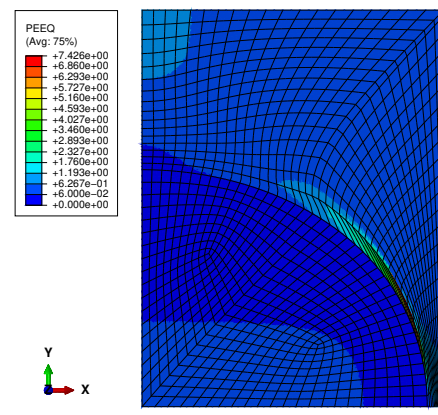


Figure 6.2.12: *Equivalent plastic strain (PEEQ) at a nominal strain of 0.2 with a) a = 1.3b and b) b = 1.3a. The color-bars are identical.*

### 6.2.4 Discussion

This study, with different changes of the geometry of the axisymmetric model show that as the geometry of the martensitic sphere changes in such a way that areas of ferrite becomes more constrained, the predicted strength increases. However, this strengthening effect does not contribute to an improvement of the predictions, but rather the opposite. As was mentioned in Chapter 3.6 the initial yielding of the martensite is dependent on the yielding of the ferrite. Thus, a too constrained ferrite is followed by a premature yielding of the martensite. This indicate that one has to be observant when modeling with higher volume fractions of martensite. It could be that this specific model should only be applied to DP steels with lower volume fractions of martensite.

However, in 6.2.2 the magnitude of the strengthening effect from this study was compared to similar results in the literature and it was found that the effect was much larger in the present work. This indicates that the over-predicted responses from the model can not only be attributed to the geometry. The description of initial yield stress, the initial strain hardening or the combination of the two is too high for the martensite.

The practical usage of this geometry of the RVE could be discussed. The DP steels are considered as isotropic materials. By modeling the martensite as an ellipsoid, the material on a macroscopic level is no longer represented as an isotropic material, but rather anisotropic and directional dependent. Since the RVE is supposed to be the smallest volume over which measurements can be performed to represent the values of the whole, the RVE of the steels should be isotropic. Hence, to model the martensite as an ellipsoid is only interesting as a mean in studying the behavior on a microscopic level, not for predicting macroscopic responses. If elongated grains are to be modeled the RVE has to be extended including more grains, elongated in different directions such that the directional effect is evened out.

## 6.3 Evaluation and validation of Single phase material model

As was stated in Chapter 6.1 the results from the micromechanical modeling indicate that the ferrite is predicted with satisfying precision. However, for the martensite better knowledge on how the parameters affect the behavior of the material is needed in order to improve the constitutive description of the material. In this section parametric studies will be performed to identify which parameters govern the plastic flow of the material. This will indicate where efforts should be made to improve the model further.

### 6.3.1 Parametric study of Ferrite grain size

The sensitivity study of the ferrite grain size, $d_f$, is done by using the extreme values in the reported range of grain sizes from the microstructure characterization, given in Table 5.1. The results are shown in Figure 6.3.1. From this it can be stated that the smallest grain size leads to an overestimation of the plastic flow, while the largest grains give an underestimation. This is physically explained, with reference to Chapter 3, by the grain boundary strengthening where smaller grains increase the total length of grain boundaries and also the increase of dislocations that origin from the volume expansion during the transformation from austenite to martensite. The single phase material model is clearly able to capture these effects. Further, the experimental results are within the spread of the numerical predictions from the reported ferrite grain sizes for all steels except DP980, which is over-predicted in the whole grain size range.
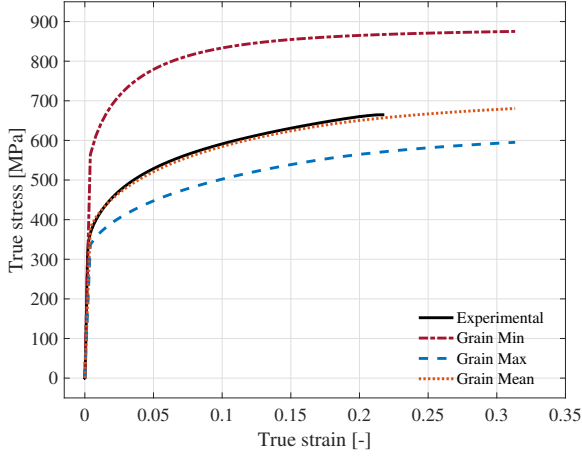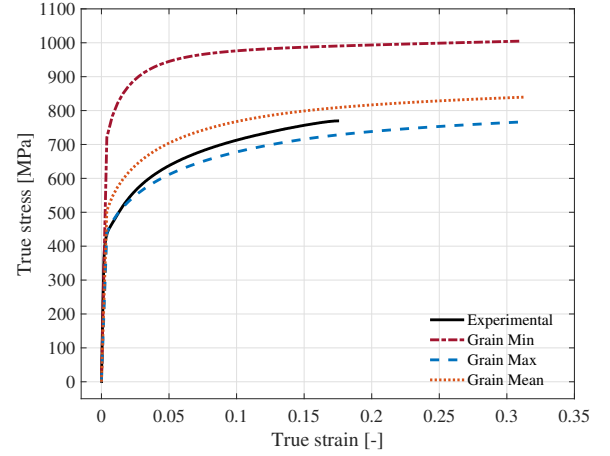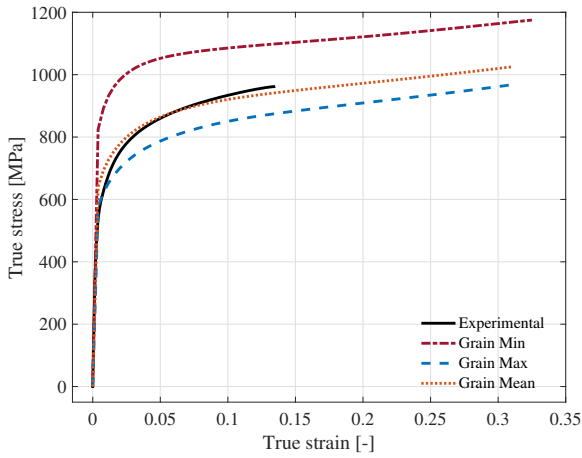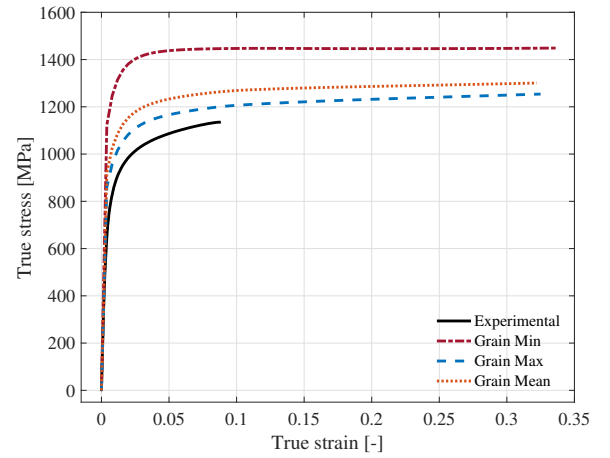
Figure 6.3.1: *Grain size variation for a) DP500, b) DP600, c) DP800 and d) DP980 with the grain sizes given in Table 5.1*

### 6.3.2 Parametric study of Carbon content

To see how and to which extent the carbon content affects the material behavior the point of supersaturation in the ferrite is changed with +/- 0.002 wt% from the value given in Chapter 5.1. The total carbon content is kept constant. As can be seen in Figure6.3.2 the variation in carbon content only has a small effect on the mechanical behavior. The total carbon content was, as described, kept constant and only carbon in ferrite, $C_f$, varied, which according to the law of mixture, Equation 5.1.2, leads to variations in carbon content of martensite, $C_m$, as well, in order to maintain the DP steel's total carbon content. However, the changes in $C_m$ will only be reflected in DP980 since no yielding of martensite occurs in DP500-DP600 and the yielding in DP800 is insignificant.

### 6.3.3 Calibration of $\Delta\sigma$

The sensitivity study of carbon did not show any large effect on the plastic flow. However, the carbon content may also influence the DP steel's strength through Equation 4.3.4 describing the solid solution strengthening from carbon, $\Delta\sigma$. The constants $P_1$ and $P_2$ in the linear
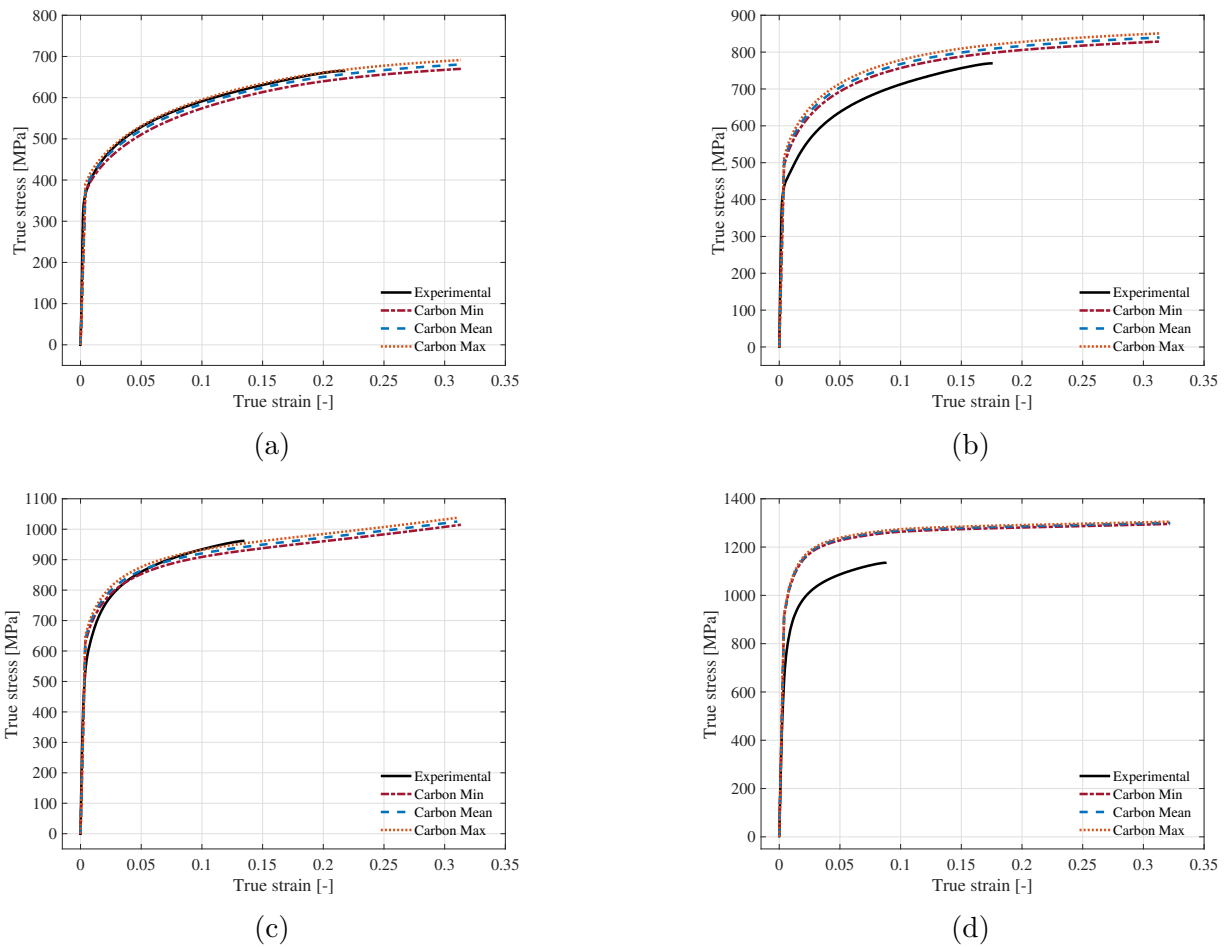
Figure 6.3.2: *Sensitivity study of carbon content for a) DP500 b) DP600 c) DP800 and d) DP980 with Carbon max $C_f$=0.01, Carbon mean $C_f$=0.008 and Carbon min $C_f$=0.006*

relation may be calibrated.

For calibration the martensitic steels are used. Since yield stress is hard to read from the stress-strain curves the ultimate tensile stress, $\sigma_{TS}$, is the property that will be used as the linkage between the martensitic steels and the martensite phase in the DP steel. As has been recognized before, the carbon content strengthens the martensite. Hence, the linear relationship between the carbon content and $\sigma_{TS}$ in the martensitic steel, which was illustrated in Figure 5.3.7, is used to find the predicted $\sigma_{TS}$ of the martensite in the DP steel.

The yield strength was then obtained by subtracting the increase in strength from strain hardening, $\sigma_h$. This value is obtained from Equation 4.3.6. From this the strengthening from carbon in solid solution had to be isolated, hence the Peierls-Naborro stress for each steel was calculated, with Equation 4.3.2. With the four values of $\Delta\sigma$ for respective steel an almost linear relation was found, when plotted against the carbon content in the martensite of the DP steels. The linear fit to these points is the calibrated equation for $\Delta\sigma$ shown in Figure 6.3.3. For comparison, the linear relation used in the base model is given in the same figure. As can be seen the calibrated $\Delta\sigma$ is lower than the one used in the base model. The effect on the prediction of the stress-strain response is given in Figure 6.3.4 for DP800 and DP980. DP500 and DP600 are not affected due to no yielding of the martensite. For DP800 the decrease in
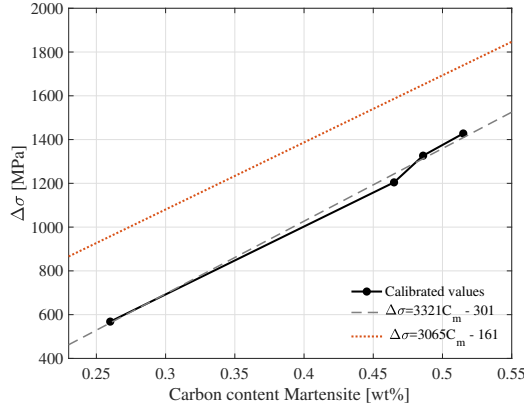
Figure 6.3.3
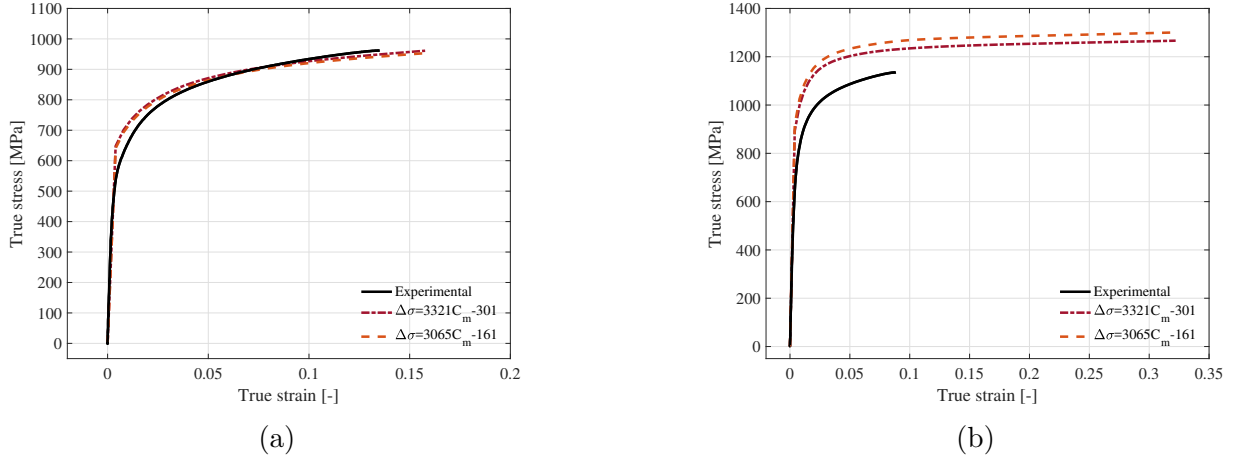


Figure 6.3.4: *Stress-strain curves with $\Delta\sigma$ calibrated and according to the literature for a) DP800 and b) DP980*

$\Delta\sigma$ results in an insignificant change in response while the point of yielding, is as expected, decreased for DP980, which accordingly leads to an improved prediction of the response.

### 6.3.4 Parametric study of Linear size of martensite

The linear size of martensite, $L_m$, is in this study and in the study by Ramazani et. al. [42] set as a constant value. In contrast to for ferrite this value is not related to the grain size. Gutierrez and Rodriguez [44] used the $L_m$ as a fitting parameter to experimental results. The best fitted values where between 0.035-0.045 $\mu m$ and was about an order of magnitude lower than the thickness of the lath size. Thus Gutierrez and Rodriguez further conclude that it seems like the linear size of martensite is not dependent on the lath size. Since the adopted value of $L_m = 0.038\ \mu m$ is based on a fitted value, a parametric study was performed where $L_m$ was changed with $+/-0.008\ \mu m$ from the value given in Table 4.1. The effect on the stress-strain curve for DP980 is shown in Figure 6.3.5. As can be seen, there is an effect of decreased ultimate tensile stress with an increased $L_m$. The initial yield stress is not affected.

51
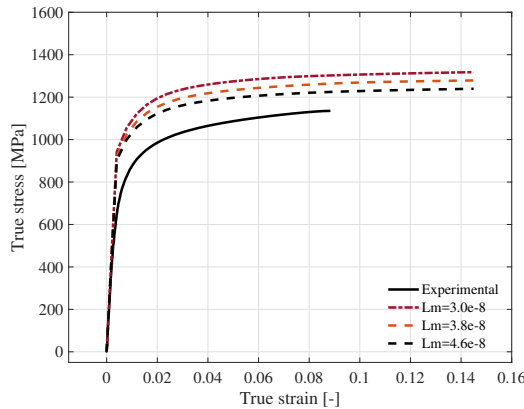
Figure 6.3.5: *Stress-strain curves with $L_m = 3e - 8$, $L_m = 3.8e - 8.5$, $L_m = 4.6e - 8$ for DP980*

## 6.3.5  Parametric study of Taylor factor

The Taylor factor describe how many favourable glide systems the crystals of the material have. When all planes and directions are possible glide system the Taylor factor is close to two [8]. The Taylor factor is, as was mentioned in Chapter 4.3 not considered as a fitting parameter. This is due to that it can be calculated for specific materials if the required data of the microstructure is retrieved. Often a simplification is done and in the literature it was found that the Taylor factor is set as three, $(M = 3)$. This is the value that so far also has been used in this work and is given in Table 4.1. However, some studies have shown or used other values for the Taylor factor. Bergström et. al. [10] use $M = 2$ in a study of both pure martensitic steel and DP steel. Tasan et. al. [50] produced EBSD-maps of a DP steel showing the Taylor factor before deformation. In this map, the Taylor factor varied between 2.05 and 3.22. Thus it was found interesting to study the magnitude of the effect of changing the Taylor factor. In Figure 6.3.6 the true stress-strain response for values of the Taylor factor $M = 2$, $M = 2.5$, $M = 3$ are given for DP980. It is found that a lower Taylor factor decrease the ultimate tensile stress and the initial yield stress to a comparatively large extent.
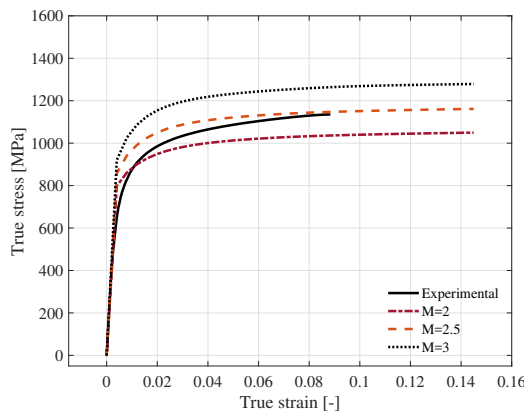


Figure 6.3.6: *Stress-strain curves with $M = 2$, $M = 2.5$, $M = 3$ for DP980*

### 6.3.6 Discussion

It is evident that the ferrite grain size does affect the response to a great extent compared to the carbon content. This is due to different factors. First, the chosen span in which the respective parameters were tested was comparatively narrower for the carbon content than for the grain sizes. This is though reasoned as an adequate difference, since the documented carbon content, in contrast to the ferrite grain sizes, is not given with a spread and is assumed to be more exact. Secondly, for ferrite, the grain size is a factor affecting both the Hall-Petch strengthening and the strain hardening since the dislocation mean free path, $L_f$, and dynamic recovery rate, $k_{rf}$ are dependent on the grain size $d_f$. Thus, both the strain dependent and independent stress are affected, which are reflected as a change in both the initial yield stress and the form of the plastic flow curve. The carbon content is only included in the strain independent part.

In the study of the ferrite grain sizes, the supposed main issue, the representation of the martensite, is not directly examined. However, it is from the results obvious that it is important to keep in mind that the offset of yielding in the martensite is strongly connected to which degree the ferrite has deformed plastically. Recall the discussion in the previous section, Section 6.2.

Further, it can from the ferrite grain size study be reasoned that all steel grades except DP980 is within the spread of numerical prediction from the range of reported grain sizes, strengthens the theory of that the ferrite is properly presented while the martensite is not.

The calibration of the strengthening from carbon in solid solution, $\Delta\sigma$, contributed to an improvement of the approximated tensile response. However, this calibration was done with the assumption that the yield stress of martensite is only dependent on $\sigma_0$ and $\Delta\sigma$. With the Hall-Petch strengthening included, the calibration would no longer be valid. Thus, this calibration should be accounted for as more qualitative than quantitative.

The study of the Linear size of martensite, $L_m$, showed that an increase in $L_m$ decreased the ultimate tensile strength. Even though the value is not based on the lath size, it reflects the effect of a refined microstructure. As has been stated before, finer structures lead to an increase in obstacles for motion of dislocations and increased strain hardening. However, even though the interval of studied values of $L_m$ is expanded from the reported span of best fits to experimental data by Gutierrez and Rodriguez [44], the effect on the stress-strain response is compared to e.g. ferrite grain size and Taylor factor, low.

The variation in values of the Taylor factor showed a large effect on the stress-strain response for DP980. This indicate that the value of the Taylor factor should be considered and that to simply adopt the value of $M = 3$ could possibly be a reason for less precise numerical predictions.

## 6.4 Ductile fracture

Due to the ductile behavior of the ferrite the most likely fracture mechanism is assumed to be ductile fracture as a consequence of nucleation, growth and coalescence of voids. To implement this in the numerical model the in Abaqus built-in model "Porous metal plasticity" can be used. This material model is based on the Gurson-Tvergaard-Needleman (GTN) damage model and the yield condition is defined according to Equation (2.1.5) described in Chapter 2.1.3.

A calibration of the GTN damage model is in this section performed, but only to illustrate

the method. Data on experimental values of strain at fracture is not available, hence the calibration is chosen to be performed with regard to the stress at necking.

The coalescence of voids is not included. Thus, the input parameters that have to be defined are the phenomenological fitting parameters $q_1$, $q_2$, $q_3$, the initial void volume fraction $f_0$ and for the fracture criteria the critical void volume fraction $f_C$ and the void volume fraction at fracture $f_F$. The q-values were chosen as proposed in Chapter 2.1.3 while the initial void volume fraction was the fitting parameter to the experimental data. Typical values of $f_C$ and $f_F$ for steels are 0.15 and 0.30 respectively, which will be used in the present work. For more information about the in-built model in Abaqus, see the Abaqus Documentation [2].

The GTN model considers strain softening. An issue with strain softening models in Abaqus and other commercial finite element codes is that energy is dissipated on a per unit volume basis. As the mesh is refined and the localization zone shrinks in size, the energy dissipation in the computation changes. Hence, prior to the fitting of the initial void volume fraction, a mesh dependence study was performed. Stress-strain curves for five different mesh sizes is presented in Figure 6.4.1. Convergence was also studied. In Figure 6.4.2, uniform elongation against number of elements in the mesh is plotted. A global convergence is obtained when approaching approximately 4000 elements. However, since the purpose of this study is only to illustrate the method, it was decided to continue with approximately 2500 elements, which is mesh 3 in Figure 6.4.1.
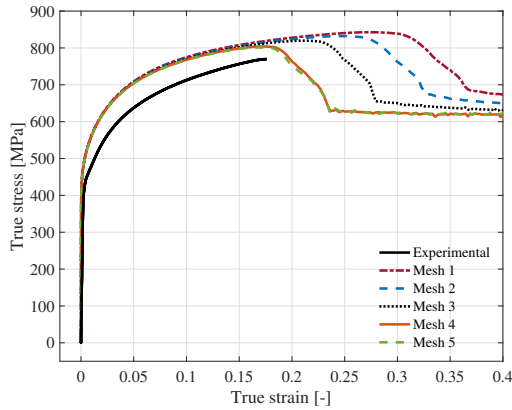


Figure 6.4.1: *True stress-strain curves with the GTN-model and with a variation of mesh sizes for DP600. The initial void volume fraction $f_0$ has a constant value of $7 \times 10^{-5}$*
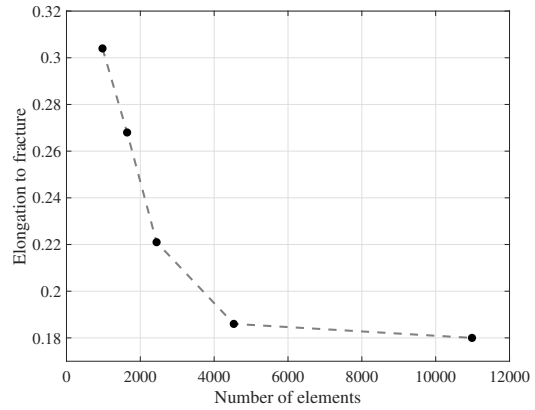
Figure 6.4.2: *Number of elements versus elongation to fracture with the GTN-model*

The obtained values of initial void volume fraction for DP500, DP600 and DP800 are given in Table 6.2. Santos et. al. [46], also applied a Gurson model to DP steels, DP600 and DP800, in a numerical model simulating a standard tensile test. They used a more comprehensive method of identifying the parameters of the GTN-model where the calibration was a four step procedure and in addition a void analysis was performed. Their results are also presented in Table 6.2. With the identified parameters in this work, the stress-strain curves in Figure 6.4.3 was obtained. DP980 is not included in the results since either no softening was initiated, or fracture occurred just as the plastic region was entered.

The initial void volume fractions are very small if comparing to the results from Santos et. al. It has to be considered that Santos et. al., in contrast to in the present work, also fitted the q-values, which affect the yield surface in a similar manner as changes in $f_0$ does. However, taking into consideration that the calibration of the GTN-model is done with respect to the stress at necking and not the elongation to fracture, the initial void volume fraction is most likely even smaller. DP steels are, as has been stated, ductile materials. Implementing coalescence of voids in the model could be a possible measure to improve the results.

Table 6.2: Initial void volume fractions and q-values both in the present work and, for comparison, from the work by Santos et. al. [46]

| | Present work | | | Santos et. al. [46] | |
|---|---|---|---|---|---|
| | DP500 | DP600 | DP800 | DP600 | DP800 |
| $f_0[\%]$ | $8 \times 10^{-5}$ | $5 \times 10^{-5}$ | $9 \times 10^{-7}$ | $5 \times 10^{-3}$ | $7 \times 10^{-3}$ |
| $q_1$ | 1.5 | 1.5 | 1.5 | 1.86 | 1.76 |
| $q_2$ | 1 | 1 | 1 | 0.8 | 0.83 |
| $q_3$ | 2.25 | 2.25 | 2.25 | 3.46 | 3.09 |

In Figure 6.4.3 contour plots of void volume fraction (VVF) are shown, which in a) is taken at the moment of fracture and in b) as the crack has propagated between the martensite and ferrite. The void initiation and growth occur at the grain boundary with a crack propagating along the phase boundary, in a similar manner for all of the three steels. These results are in line with the results found by Gurland and Szewczyk [49] and [29] where in the former the void formation due to decohesion of the martensite-ferrite interface was the only present mechanism and in the latter the same mechanism was found for globular martensite, which is the assumed morphology in the present axisymmetric model. Plastic strain localization and high triaxiality are the most important factors governing the initiation of ductile fracture. In Figure 6.4.5 contour plots of the equivalent plastic strain and the triaxiality are shown. Both PEEQ and TRIAX are highest along the grain boundary and in the direction of the crack propagation. As was also stated in Chapter 3.8, the type of fracture mode depends on the volume fraction of martensite, where it was reported that smaller volume fractions of martensite lead to both decohesion of the martensite-ferrite interface and martensite cracking, while for larger volume fractions of martensite, martensite cracking was the only failure mode. Thus, it would be interesting in further studies to implement brittle fracture models for DP steels with high volume fractions martensite. Uthaisangsuk et. al. [55] propose brittle fracture models as Beremin local criterion, cohesive zone model and XFEM to model cleavage of martensite.

For conclusion, even though no quantitative results are obtained from this study, the method of calibration and the initiation and growth of voids along the martensite- ferrite interface can be illustrated.
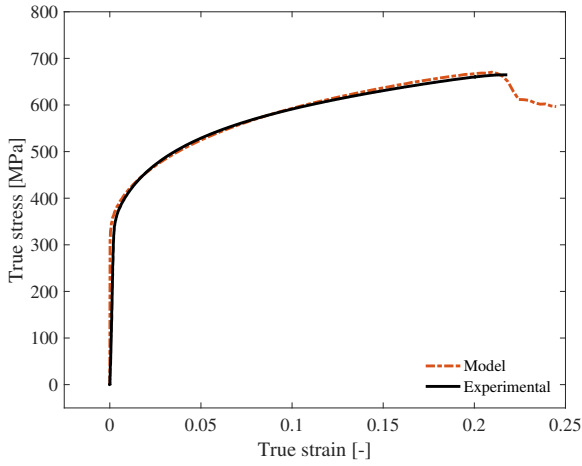
(a) *DP500*
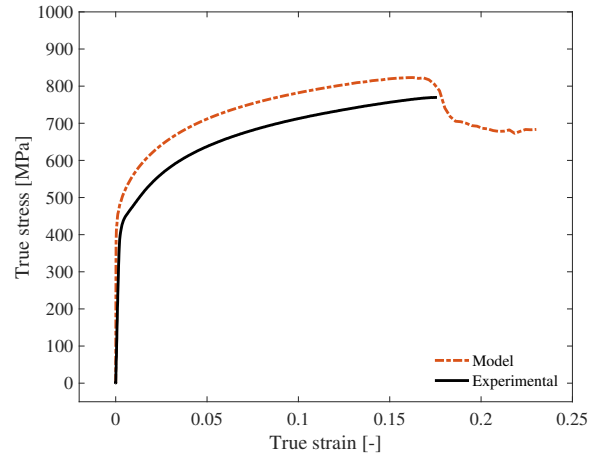
(b) *DP600*
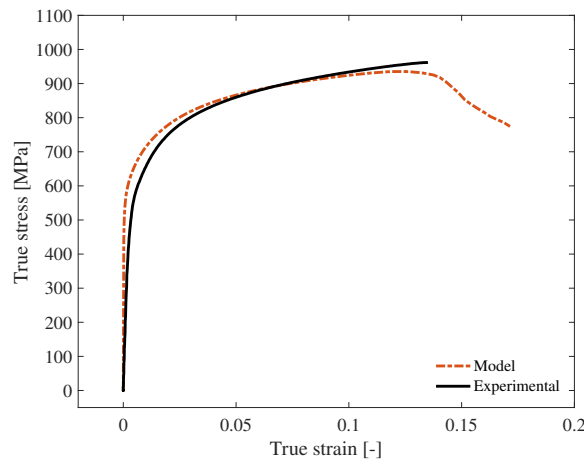
(c) *DP800*

Figure 6.4.3: *True stress-strain curves with the GTN-model implemented compared to experimental response for a) DP500, b) DP600 and c) DP800*
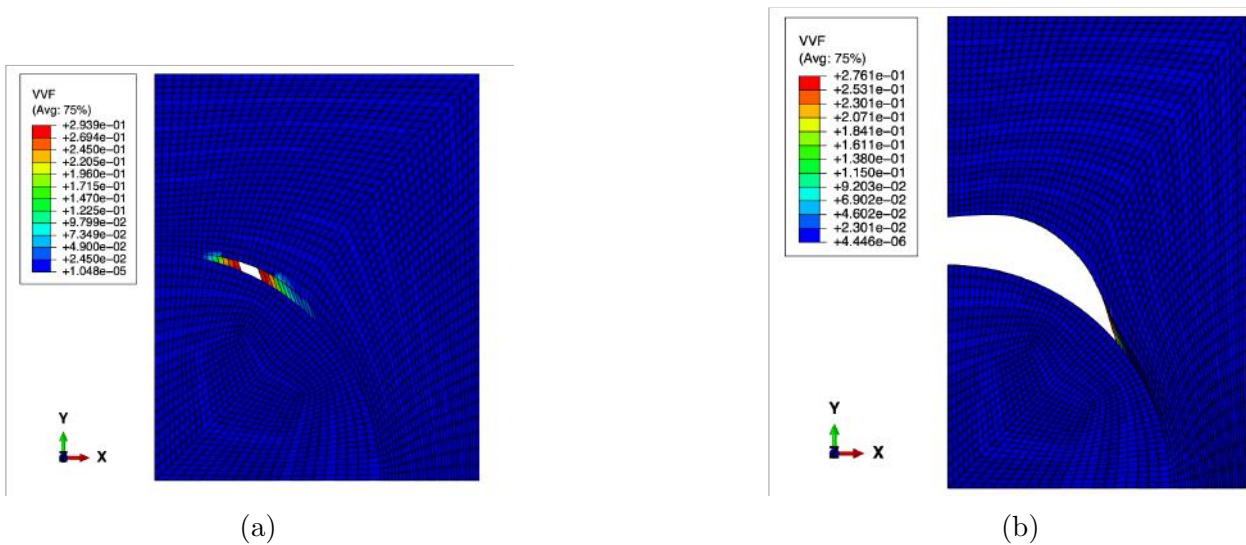


(a)

(b)

Figure 6.4.4: *Void volume fraction (VVF) in DP600 at a true strain of a) 0.16 - Crack initiation (b) 0.37 - Crack propagation along the phase boundary*
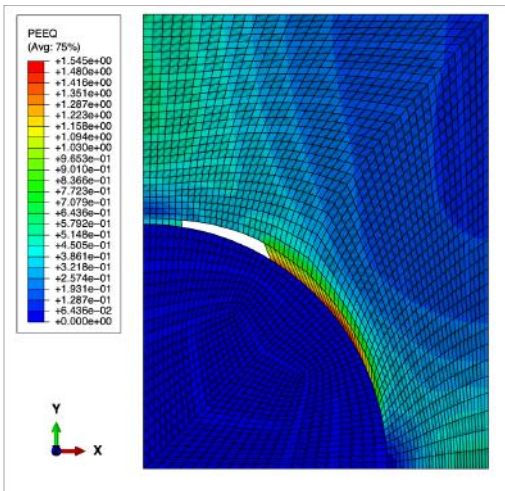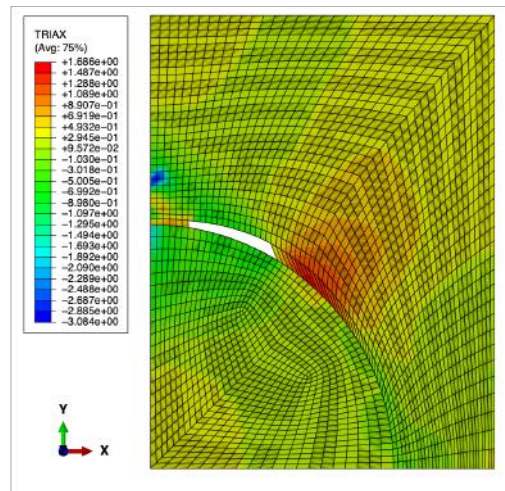
(a)                                                    (b)

Figure 6.4.5: *For DP600 a) Equivalent plastic strain (PPEQ) and b) Triaxiality (TRIAX)*

57

# CHAPTER 7

## Conclusions

Four DP steels, DP500, DP600, DP800 and DP980, have in this work been studied with regard to microstructure and plastic response in uniaxial tension. A micromechanical model framework predicting the mechanical behavior of the steels was applied in simulations of DP steels and evaluated.

The micromechanical model primarily consists of two parts, the representative volume element in the form of an axisymmetric model and the single phase material model for respective phase. A base model was first set up with dimensions of the axisymmetric model and values of the parameters in the, so-called, single phase material model according to the literature. From the base model the axisymmetric model and the single phase material model were studied separately in order to evaluate and validate each part. Conclusions that can be drawn from the results and discussions are:

- Good agreement between the experimental and the predicted response is obtained for DP500 and DP800. The predicted response for DP600 is less precise and DP980 is significantly over-predicted. In DP500 and DP600 only the ferrite experiences plastic deformation, while in DP800 plastic deformation is at the start of extending from the ferrite to the martensite and in DP980 plastic deformation of martensite is excessively spread.

- By varying the geometry of the axisymmetric model in the Double model and the Ellipsoid model a strengthening effect was seen. This strengthening was not advantageous with respect to the intention to improve the predictions of tensile response of the steels. The common phenomena found for all results where the model over-predicted the response was that the radius of the martensitic sphere was increased in at least one direction in such a way that the ferrite got more constrained. Thus, the conclusion that can be drawn is that the model is more suitable when modeling steels with smaller volume fractions of martensite. In fact, the model is not at all applicable for steels with only a small increase in volume fraction martensite from that in DP980.

- The particle size effect in the study of the Double-model was compared to results from the literature. The trends correlated but the magnitude of the effect was larger in the

present work. This indicate that the over-predictions can not solely be appertained to geometrical effects, but also that the work-hardening of the martensite is not properly represented.

- The previous conclusion was strengthened by the study of ferrite grain sizes. By varying the ferrite grain size within the reported spread it was evident that the experimental response was within the spread of predictions with the different grain sizes for all the steel-grades except for DP980. This result also makes it possible to assume that the less precise prediction for DP600 from the base model is due to uncertainties in the microstructural data.

- The single phase material model for ferrite is strongly dependent on the ferrite grain size, since it is assumed that both dynamic recovery rate and dislocation mean free path are dependent on the grain size. It is therefore important to make sure that the microstructure is properly characterized since only small variations in the grain size will give pronounced effects.

- The strengthening from solid solution of carbon is given by a linear relationship. This relationship was calibrated as an attempt to improve the constitutive model of the martensite. For the calibration, martensitic steels were used. The calibration provided an improvement by lowering the yield stress. However the calibration was done with the assumption that the initial yield stress is only dependent on two mechanism. If the Hall-Petch grain boundary strengthening would have been included, the calibration would no longer be valid.

- The study of the single phase material model gives a magnitude of the effect from changes in the values of parameters included. This provides an indication on where efforts should primarily be made to find the true values of the parameters in order to improve the numerical predictions the most. However, the study do not include any quantitative evaluation of the parameters. For that, more information, primarily on the intrinsic structure of the martensite, is needed.

- A demonstration of the modeling of ductile fracture by implementing a Gurson-Tvergaard-Needleman material model was done. The study was only qualitative since the calibration of the model was done with respect to the stress at necking. However, a realistic illustration of void initiation and growth along the ferrite-martensite interface was obtained.

# CHAPTER 8

## Future work

The work has been limited in different ways, hence there still remain further investigations to perform and analysis work to conduct in order to gain more knowledge about the material and how to model it. Some relevant suggestions of such are presented in this chapter.

- As has been stated in previous chapter, high volume fractions of martensite lead to over-prediction of the plastic flow. Thus a better understanding of the martensite morphology is needed. How should the grain size and linear size of martensite be accounted for? The microstructure of the martensitic steel should be characterized. Tests on pure ferritic steels would enable a separation of the ferrite from the martensite. The grain boundary between the ferrite and martensite is the most active area and the strengthening mechanisms connected to this area could be isolated if each phase was tested separately.

- Valuable information about the martensite could also be obtained from additional hardness tests of the DP steels with a higher indentation load, since the load applied in the existing results, according to the literature, is too low.

- Since DP steels are complex materials with multiple parameters affecting the material at the same time the parameters should be isolated and studied one by one. For instance the carbon content in the martensite could be kept constant as the volume fraction martensite increased or the volume fraction martensite could be varied as the ferrite grain size was constant.

- For further validation of the micromechanical model, cyclic loading and the Bauschinger effect could be studied. This would require experimental compression-tension tests.

- To investigate if the over-prediction of the DP980 has to do with the constitutive model or the geometry of the RVE a more complex 3D-model should be established where the same constitutive model as in this work is applied.

# References

[1]   G. S. M. A Goel R K Ray. "Bauschinger effect in a dual-phase steel". *Scripta Metallurgical* 17 (1983). DOI: `10.1016/0036-9748(83)90176-X`.

[2]   *Abaqus Analysis User's Manual. 20.2.9 Porous Metal Plasticity.* Version 6.10. Dassault Systèmes, 2010. URL: `https://www.sharcnet.ca/Software/Abaqus610/Documentation/docs/v6.10/books/usb/default.htm?startat=pt05ch20s02abm24.html`.

[3]   F. M. Al-Abbasi and J. A. Nemes. "Characterizing DP-steels using micromechanical modeling of cells". *Computational Materials Science* 39 (2007), pp. 402–415.

[4]   F. M. Al-Abbasi and J. A. Nemes. "Micromechanical modeling of the effect of particle size difference in dual phase steels". *International Journal of Solids and Structures* 40 (2003), pp. 3379–3391.

[5]   F. M. Al-Abbasi and J. A. Nemes. "Predicting the Ductile Failure of DP-steels Using Micromechanical Modeling of Cells". *International Journal of DAMAGE MECHANICS* 17 (2008). DOI: `10.1177/1056789507077441`.

[6]   T. L. Anderson. *Fracture Mechanics: Fundamentals and Applications.* Boca Raton: Taylor and Francis, 2011.

[7]   A. S. Argon, J. Im, and R. Safoglu. "Cavity Formation from Inclusions in Ductile Fracture". *Metallurgical Transactions* 6A (2017), pp. 825–837.

[8]   J. Back and G. Engberg. "Investigation of Parent Austenite Grains from Martensite Structure Using EBSD in a Wear Resistant Steel". *Materials (Basel)* 10(5) (2017), p. 453.

[9]   G. Béres and Z. Weltsch. "Estimation of Strength Properties from Microhardness Results in Dual Phase Steels with Different Martensite Volume Fraction". *Periodica Polytechnica Transportation Engineering* (2018). DOI: `https://doi.org/10.3311/PPtr.12113`.

[10]  Y. Bergström. *The plastic deformation process of metals - 50 years development of a dislocation based theory.* 2015. URL: `https://www.metalliskamaterial.se/globalassets/4-fakta/artiklarrapporter/yngve-bergstrom/yngve-bergstrom-eng-the-plastic-deformation-process-of-metals.pdf`. accessed: 02.06.2019.

[11]  C. Butcher et al. "Damage Evolution in Complex-Phase and Dual-Phase Steels during Edge Stretching". *Materials (Basel)* 10 (2017), p. 346. DOI: `10.3390/ma10040346`.

[12] M. Calcagnotto et al. "Deformation and fracture mechanisms in fine- and ultrafine-grained ferrite/martensite dual-phase steels and the effect of aging". *Acta Materialia 59* 2011 (2011), pp. 658–670. DOI: 10.1016/j.actamat.2010.10.002.

[13] M. Calcagnotto et al. "Orientation gradients and geometrically necessary dislocations in ultrafine grained dual-phase steels studied by 2D and 3D EBSD". *Materials Science and Engineering: A* 527 (2010), pp. 2738–2746.

[14] F. C. Campbell. *Elements of Metallurgy and Engineering Alloys*. Ohio: ASM International Press, 2008.

[15] N. R. Center. *Introduction to Materials and Processes*. 2014. URL: https://www.nde-ed.org/EducationResources/CommunityCollege/Materials/Structure/linear_defects.htm.

[16] P.-H. Chang and A. G. Preban. "The effect of ferrite grain size and the martensite volume fraction on the tensile properties of dual phase steel". *Acta Metall* 33(5) (1984), pp. 897–903.

[17] D. Chatterjee. "Behind the Development of Advanced High Strength Steel (AHSS) Including Stainless Steel for Automotive and Structural Applications - An Overview". *Materials Science and Metallurgy Engineering* 4 (2017), pp. 1–15.

[18] K. K. Chawla. *Mechanical Behaviour of Materials, Second Edition*. Cambridge University Press, 2009. Chap. 3.4.

[19] V. L. Concepcion, H. N. Lorusso, and H. G. Svoboda. "Effect of carbon on microstructure and mechanical properties of dual phase steels". *Procedia Material Science* 8 (2013), pp. 1047–1056.

[20] E. Fagerholt. "Field measurements in mechanical testing using close-range phtogrammetry and digital image analysis". PhD thesis. Trondheim: Norwegian University of Science and Technology, 2012.

[21] N. Fonstein. *Automotive Steels - Design, Metallurgy, Processing and Applications*. Woodhead Publishing, 2017. Chap. 7, pp. 169–216. (Visited on 03/15/2019).

[22] Y. Granbom. "Structure and mechanical properties of dual phase steels: An experimental and theoretical analysis". PhD thesis. Stockholm: Royal Institute of Technology, 2010.

[23] A. L. Gurson. "Continuum Theory of Ductile Rupture by Void Nucleation and Growth: Part I—Yield Criteria and Flow Rules for Porous Ductile Materials". *Journal of Engineering Materials and Technology* 99 (1977), pp. 2–15.

[24] S. R. Hiremath, D. Alapus, and D. R. Mahapatra. *Blast Mitigation Strategies in Marine Composite and Sandwich Structures*. Singapore: Springer, 2018. Chap. Stress Triaxiality in Damage Models.

[25] O. S. Hopperstad and T. Børvik. *Impact Mechanics. Part II. Lecture Notes*. Trondheim: Norwegian University of Science and Technology, 2017.

[26] O. S. Hopperstad and T. Børvik. *Material Mechanics. Part I. Lecture Notes*. Trondheim: Norwegian University of Science and Technology, 2017.

[27] Y. Hou. "Modelling of plasticity and fracture behaviors of dual-phase steel". PhD thesis. Compiègne: Université de Technologie de Compiègne, 2016.

[28] I. S. Kim and T. S. Byun. "Tensile properties and inhomogeneous deformation of ferrite-martensite dual-phase steels". *Journal of Material Science* 28 (1993), pp. 2923–2932.

[29] N. J. Kim and G. Thomas. "Effect of Morphology on the Mechanical Behavior of Dual Phase Fe/2Si/0.1C Steel". *Metallurgical Transactions* 12(A) (1981), pp. 483–488.

[30]   G. Krauss and D. L. Steinbrunner. "Void Formation during Tensile Testing of Dual Phase Steels". *Metallurgical Transactions* 9(A) (1988), pp. 579–589.

[31]   Q. Lai et al. "Influence of martensite volume fraction and hardness on the plastic behaviour of dual-phase steels: Experiments and micromechanical modeling". *International Journal of Plasticity* 80 (2015), pp. 187–203.

[32]   C. Landron. "Ductile damage characterization in Dual-Phase steels using X-ray tomography". PhD thesis. Lyon: INSA-Lyon, 2011. (Visited on 03/17/2019).

[33]   Y. Mazaheri, A. Kermanpur, and A. Najafizadeh. "Strenghtening Mechansisms of Ultra-fine Grained Dual Phase Steels Developed by New Thermomechanical Processing". *ISIJ International* (2014). DOI: 10.2355/isijinternational.55.218.

[34]   M. Mazinani and W. Poole. "Effect of Martensite Plasticity on the Deformation Behavior of a Low-Carbon Dual-Phase Steel". *Metall and Mat Trans A* (2007). DOI: https://doi.org/10.1007/s11661-006-9023-3.

[35]   B. McGinty. *Continuum Mechanics*. URL: https://www.continuummechanics.org/index.html. accessed: 04.06.2019.

[36]   L. Nyborg and Y. Cao. *Course summary: Basics - strengthening of metals*. Gothenburg: Chalmers School of Technology, 2018.

[37]   C. O. Paulsen. "DP steels - microstructure summary". Unpublished. 08-02-2019.

[38]   M. J. Perez. "DP steels". Unpublished. 29-01-2019.

[39]   N. J. Petch. "The Cleavage Strength of Polycrystals". *The Journal of the Iron and Steel Institute* 173(5) (1953), pp. 25–28.

[40]   A. P. Pierman et al. "The influence of microstructure and composition on the plastic behaviour of dual-phase steels". *Acta Materialia* 73 (2014), pp. 298–311.

[41]   A. Ramazani et al. "Correlation between 2D and 3D flow curve modelling of DP steels using a microstructure-based RVE approach". *Materials Science and Engineering: A* 560 (2013), pp. 129–139.

[42]   A. Ramazani et al. "Modelling the effect of microstructural banding on the flow curve behaviour of dual-phase steels". *Computational Material Science* 52 (2011), pp. 46–54.

[43]   A. C. Reardon. *Metallurgy for the Non-Metallurgist, Second Edition*. Ohio: ASM International Press, 2011.

[44]   R. M. Rodriguz and I. Gutierrez. "Unified Formulation to Predict the Tensile Curves of Steels with Different Microstructures". *skipbib=true* 426-432 (2003), pp. 4525–4530.

[45]   A. Saai. "SINTEF$_M$M5$_r$eport$_2$018". Unpublished. 15-02-2019.

[46]   R. O. Santos et al. "Damage identification parameters of dual-phase 600–800 steels based on experimental void analysis and finite element simulations". *Journal of Materials Research and Technology* 8(1) (2019), pp. 644–659.

[47]   X. Sun et al. "In uence of martensite mechanical properties on failure mode and ductility of dual-phase steels". *Metall. Mater. Trans.* 40A (2009), pp. 796–810.

[48]   X. Sun et al. "Predicting failure modes and ductility of dual phase steels using plastic strain localization". *International Journal of Plasticity* 25 (2009), pp. 1888–1909.

[49]   A. F. Szewczyk and J. Gurland. "A Study of The Deformation and Fracture of a Dual-Phase Steel". *Metallurgical Transactions* 13(A) (1982), pp. 1821–1826.

[50]   C. C. Tasan et al. "Strain localization and damage in dual phase steels investigated by coupled in-situ deformation experiments and crystal plasticity simulations". *International Journal of Plasticity* 63 (2014), pp. 198–210.

[51] C. Thomser, V. Uthaisangsuk, and W. Bleck. "Influence of Martensite Distribution on the Mechanical Properties of Dual Phase Steels: Experiments and Simulation". *Steel Research International* 80 (2009).

[52] H. Toda et al. "Damage micromechanisms in dual-phase steel investigated with combined phase- and absorption-contrast tomography". *Acta Materialia* 133 (2017), p. 441. DOI: https://doi.org/10.1016/j.actamat.2017.01.010.

[53] V. Tvergaard. "On localization in ductile materials containing spherical voids". *International Journal of Fracture Mechanics* 18 (1982), pp. 237–252.

[54] V. Uthaisangsuk, U. Prahl, and W. Bleck. "Stretch-flange ability characterisation of multiphase steel using a microstructure based failure modelling". *Computational Materials Science* 45 (2009), pp. 617–623.

[55] V. Uthaisangsuk et al. "A micromechanical damage simulation of dual phase steels using XFEM". *Computational Materials Science* 54 (2012), pp. 271–279.

[56] V. Uthaisangsuk et al. "A study of microcrack formation in multiphase steel using representative volume element and damage mechanics". *Computational Materials Science* 50 (2011), pp. 1225–1232.

[57] V. Uthaisangsuk et al. "Experimental and numerical failure criterion for formability prediction in sheet metal forming". *Computational Materials Science* 43 (2008), pp. 43–50.

# APPENDIX A

Inputfile example

```
*Heading
** Job name: DP500job Model name: Micromech
** Generated by: Abaqus/CAE 6.14-4
*Preprint, echo=YES, model=YES, history=YES, contact=YES
**
** PARTS
**
*Part, name=Axisym
*Node
      1,    42.0021439,    42.0021439
      2,            0.,    59.4000015
      3,            0.,            0.
      4,          100.,          100.
      5,            0.,          100.
..... ..... ..... ..... .....
..... ..... ..... ..... .....

*Element, type=CAX8R
  1,    24,    25,    306,    290, 2607, 2608, 2609, 2610
  2,    25,    26,    307,    306, 2611, 2612, 2613, 2608
  3,    26,    27,    308,    307, 2614, 2615, 2616, 2612
  4,    27,    28,    309,    308, 2617, 2618, 2619, 2615
  5,    28,    29,    310,    309, 2620, 2621, 2622, 2618
..... ..... ..... ..... .....
..... ..... ..... ..... .....

*Nset, nset=Martensite
    1,     2,     3,     6,     9,    10,    11,    12,    13,    14,    15,
16,    17,    18,    19,    20
   21,    22,    23,    24,    25,    26,    27,    28,    29,    30,    31,
32,    33,    34,    35,
..... ..... ..... ..... .....
..... ..... ..... ..... .....

*Elset, elset=Martensite
    1,     2,     3,     4,     5,     6,     7,     8,     9,    10,    11,
12,    13,    14,    15,    16
   17,    18,    19,    20,    21,    22,    23,    24,    25,    26,    27,
28,    29,    30,    31,
..... ..... ..... ..... .....
..... ..... ..... ..... .....

*Nset, nset=Ferrite
    1,     2,     4,     5,     6,     7,     8,    34,    35,    36,    37,
38,    39,    40,    41,    42
   43,    44,    45,    46,    47,    48,    49,    50,    51,    52,    53,
54,    55,    56,    57,
..... ..... ..... ..... .....
..... ..... ..... ..... .....

*Elset, elset="Edge Seeds-2"
   10,    20,    30,    40,    50,    60,    70,    80,    90,   100,   110,
120,   130,   140,   150,   151
  152,   153,   154,   155,   156,   157,   158,   159,   160,   161,   162,
```

```
163,  164,  165,  166,
..... ..... ..... ..... .....
..... ..... ..... ..... .....

** Section: Martensite
*Solid Section, elset=Martensite, controls=EC-1, material=Martensite
1.,
** Section: Ferrite
*Solid Section, elset=Ferrite, controls=EC-1, material=Ferrite
1.,
*End Part
**
**
** ASSEMBLY
**
*Assembly, name=Assembly
**
*Instance, name=Axisym-1, part=Axisym
*End Instance
**
*Nset, nset=Bottom, instance=Axisym-1
    3,    6,    8,  162,  163,  164,  165,  166,  167,  168,  169,
 170,  171,  172,  173,  174
  175,  176,  177,  178,  179,  180,  181,  182,  183,  184,  185,
 216,  217,  218,  219,
..... ..... ..... ..... .....
..... ..... ..... ..... .....

*Elset, elset=Bottom, instance=Axisym-1
 1264, 1265, 1266, 1267, 1268, 1269, 1270, 1271, 1272, 1273, 1589,
1605, 1621, 1637, 1653, 1669
 1685, 1701, 1717, 1733, 1749, 1765, 1781, 1797, 1813, 1844, 1875,
1906, 1937, 1968, 1999,
..... ..... ..... ..... .....
..... ..... ..... ..... .....

*Nset, nset=ConstraintNodes, instance=Axisym-1
    7,    8,  238,  239,  240,  241,  242,  243,  244,  245,  246,
 247,  248,  249,  250,  251
  252,  253,  254,  255,  256,  257,  258,  259,  260,  261,  262,
 263,  264,  265,  266,
..... ..... ..... ..... .....
..... ..... ..... ..... .....

*Elset, elset=ConstraintNodes, instance=Axisym-1, generate
 2497,  2526,     1
*Nset, nset=Diagonal, instance=Axisym-1
    1,    4,   88,   89,   90,   91,   92,   93,   94,   95,   96,
  97,   98,   99,  100,  101
  102,  103,  104,  105,  106,  107,  108,  109, 3809, 3872, 3935,
3998, 4061, 4124, 4187,
..... ..... ..... ..... .....
..... ..... ..... ..... .....
```

*Elset, elset=Diagonal, instance=Axisym-1
  581,  612,  643,  674,  705,  736,  767,  798,  829,  860,  891,
922,  953,  984, 1015, 1046
 1077, 1108, 1139, 1170, 1201, 1232, 1263, 1814, 1845, 1876, 1907,
1938, 1969, 2000, 2031,
..... ..... ..... ..... .....
..... ..... ..... ..... .....

*Nset, nset=Rightside, instance=Axisym-1
    7,    8,  238,  239,  240,  241,  242,  243,  244,  245,  246,
247,  248,  249,  250,  251
  252,  253,  254,  255,  256,  257,  258,  259,  260,  261,  262,
263,  264,  265,  266,
*Elset, elset=Rightside, instance=Axisym-1, generate
 2497, 2526,    1
..... ..... ..... ..... .....
..... ..... ..... ..... .....

*Nset, nset=Masternode, instance=Axisym-1
 4,
*Nset, nset=Symline, instance=Axisym-1
    2,    3,    5,   64,   65,   66,   67,   68,   69,   70,   71,
72,   73,   74,   75,   76
   77,   78,   79,   80,   81,   82,   83,   84,   85,   86,   87,
140,  141,  142,  143,
..... ..... ..... ..... .....
..... ..... ..... ..... .....

*Elset, elset=Symline, instance=Axisym-1
  166,  182,  198,  214,  230,  246,  262,  278,  294,  310,  311,
312,  313,  314,  315,  316
  317,  318,  319,  320,  321,  322,  323,  324,  325,  551,  582,
613,  644,  675,  706,
..... ..... ..... ..... .....
..... ..... ..... ..... .....

*Nset, nset=Top, instance=Axisym-1
    4,    5,  110,  111,  112,  113,  114,  115,  116,  117,  118,
119,  120,  121,  122,  123
  124,  125,  126,  127,  128,  129,  130,  131,  132,  133,  134,
135,  136,  137,  138,
..... ..... ..... ..... .....
..... ..... ..... ..... .....

*Elset, elset=Top, instance=Axisym-1, generate
 1233, 1263,    1

** Constraint: VerticalRight
*Equation
2
ConstraintNodes, 1, 1.
Masternode, 1, -1.

*End Assembly

```
**
** ELEMENT CONTROLS
**
*Section Controls, name=EC-1, ELEMENT DELETION=YES
1., 1., 1.
*Amplitude, name=Amp-1
            0.,            0.,            1.,            1.
*Amplitude, name=Amp-2, definition=SMOOTH STEP
            0.,            0.,            1.,            1.
**
** MATERIALS
**
*Material, name=Ferrite
*Elastic
 2.1e+06, 0.33
*Plastic
 304.171,         0.
  331.51, 0.00133779
 342.789, 0.00267559
 351.412, 0.00401338
 358.655, 0.00535117
..... ..... ..... ...... .....
..... ..... ..... ...... .....
 648.423,   0.394649
 648.688,   0.395987
 648.952,   0.397324
 649.214,   0.398662
 649.475,        0.4

*Material, name=Martensite
*Elastic
 2.1e+06, 0.33
*Plastic
 1568.91,         0.
  1959.7, 0.00133779
 2100.19, 0.00267559
 2195.13, 0.00401338
 2265.59, 0.00535117
..... ..... ..... ...... .....
..... ..... ..... ...... .....
 2572.17,   0.394649
 2572.17,   0.395987
 2572.17,   0.397324
 2572.17,   0.398662
 2572.17,        0.4

**
** BOUNDARY CONDITIONS
**
** Name: Bottom Type: Symmetry/Antisymmetry/Encastre
*Boundary
Bottom, YSYMM
** Name: Symline Type: Symmetry/Antisymmetry/Encastre
*Boundary
```

```
Symline, XSYMM
** ----------------------------------------------------------------
**
** STEP: Loading
**
*Step, name=Loading, nlgeom=YES
*Static
1., 1., 1e-05, 1.
**
** BOUNDARY CONDITIONS
**
** Name: Prescribed_def Type: Displacement/Rotation
*Boundary
Top, 2, 2, 40.
**
** OUTPUT REQUESTS
**
*Restart, write, frequency=0
**
** FIELD OUTPUT: F-Output-1
**
*Output, field, variable=PRESELECT, time interval=0.01
**
** HISTORY OUTPUT: H-Output-1
**
*Output, history, variable=PRESELECT
**
** HISTORY OUTPUT: PEEQ
**
*Output, history, frequency=99999
*Element Output, elset=Diagonal
PEEQ,
**
** HISTORY OUTPUT: Reaction
**
*Output, history, number interval=100
*Node Output, nset=Bottom
RF1, RF2
**
** HISTORY OUTPUT: Displacement
**
*Node Output, nset=Masternode
U1, U2
*End Step
```

# APPENDIX B

Martensitic steel data

| Sheet material | Reference | Original sheet dimensions (m) | Chemical compositions (% wt) | | | | | |
|---|---|---|---|---|---|---|---|---|
| | | | C | Mn | Si | NB | Ti | B |
| Doc 1200 M | C30436 | 1.37 × 1.25 × 0.001 | 0,113 | 1,6 | 0,21 | 0,016 | | |
| Doc 1400 M | C78513 | 2 × 1.25 × 0.001 | 0,175 | 1,3 | 0,20 | | 0,033 | 0,002 |
| Doc 1700 M | C35119 | 2 × 1.25 × 0.001 | 0,271 | 0,5 | 0,21 | | 0,034 | 0,002 |

| | | | | | | | | | | | | | | | | | |
|---|---|---|---|---|---|---|---|---|---|---|---|---|---|---|---|---|---|
| Duration of test load: | | 10s | | Instrument: Leica VMHT MOT | | | Sample 1200 prepared to SiC#2000, sample 1400 and 1700 prepared to SiC#4000 | | | | | | | | | | |
| Load [kgf] | 0,01 | 0,1 | | | | | | | | | | | | | | | |
| Sample | 1200 | | | | 1400 | | | | | 1700 | | | | | | | |
| Sample thickness | 0,98 | mm | | | 0,91 | mm | | | | 0,97 | mm | | | | | | |
| | | HMV beregnet | d1 [µm] | d2 [µm] | Δd [%] | | | | | | HMV beregnet | d1 [µm] | d2 [µm] | Δd [%] | | | |
| | HMV0,01 | | | | | HMV0,01 | HMV beregnet | d1 [µm] | d2 [µm] | Δd [%] | | | | | HMV0,01 | | |
| | 14,6 | 14,5625 | 35,57 | 35,8 | 0,66 | 12,8 | 12,7751 | 38,3 | 37,9 | 0,82 | 9,5 | 9,4928 | 43,80 | 44,60 | 1,89 | | |
| | 11,8 | 11,8107 | 39,82 | 39,43 | 1 | 10,7 | 10,6900 | 41,8 | 41,5 | 0,59 | 9,3 | 9,2602 | 44,60 | 44,90 | 0,73 | | |
| | 11,1 | 11,1350 | 40,53 | 41,09 | 1,37 | 7,89 | 7,8835 | 48,4 | 48,6 | 0,35 | 9,1 | 9,0580 | 44,70 | 45,80 | 2,45 | | |
| | 8,5 | 8,4975 | 46,74 | 46,69 | 0,1 | 4,92 | 4,9269 | 61,5 | 61,2 | 0,49 | 9,0 | 8,9578 | 45,80 | 45,20 | 1,23 | | |
| | 10,2 | 10,2304 | 42,53 | 42,62 | 0,21 | 10,6 | 10,6388 | 41,7 | 41,8 | 0,12 | 9,0 | 8,9973 | 45,10 | 45,70 | 1,26 | | |
| | 10,9 | 10,8725 | 41,62 | 40,98 | 1,56 | 9,69 | 9,6884 | 43,6 | 43,9 | 0,62 | 9,1 | 9,0767 | 45,30 | 45,10 | 0,37 | | |
| Average | 11,2 | 11,2 | 41,1 | 41,1 | 0,8 | 9,4 | 9,4 | 45,9 | 45,8 | 0,5 | 9,1 | 9,1 | 44,9 | 45,2 | 1,3 | | |
| | HMV0,1 | | d1 [µm] | d2 [µm] | Δd [%] | HMV0,1 | | d1 [µm] | d2 [µm] | Δd [%] | HMV0,1 | | d1 [µm] | d2 [µm] | Δd [%] | | |
| | 384,0 | 384,3670 | 21,89 | 22,04 | 0,65 | 499 | 497,8522 | 19,2 | 19,4 | 0,81 | 585,0 | 585,2796 | 17,8 | 17,8 | 0,37 | | |
| | 372,0 | 371,7745 | 22,1 | 22,57 | 2,1 | 497 | 497,9592 | 19,6 | 19 | 2,83 | 574,0 | 585,2796 | 17,8 | 17,8 | 0 | | |
| | 372,0 | 371,7348 | 22,38 | 22,29 | 0,44 | 483 | 482,7155 | 19,6 | 19,6 | 0,07 | 603,0 | 602,0779 | 17,6 | 17,5 | 0,82 | | |
| | 363,0 | 363,3890 | 22,62 | 22,56 | 0,29 | 470 | 468,3183 | 20,1 | 19,7 | 2,1 | 611,0 | 612,5186 | 17,5 | 17,3 | 1,2 | | |
| | 357,0 | 357,1178 | 22,45 | 23,13 | 2,97 | 489 | 487,6920 | 19,4 | 19,6 | 1,2 | 591,0 | 591,9116 | 17,7 | 17,7 | 0,22 | | |
| | 361,0 | 361,2233 | 22,99 | 22,33 | 2,93 | 479 | 478,0244 | 20,1 | 19,3 | 3,91 | 637,0 | 637,9085 | 17 | 17,1 | 0,46 | | |
| Average | 368,2 | 368,3 | 22,4 | 22,5 | 1,6 | 486,2 | 485,4 | 19,7 | 19,4 | 1,8 | 600,2 | 602,5 | 17,6 | 17,5 | 0,5 | | |
| | HMV1 | | d1 [µm] | d2 [µm] | Δd [%] | HMV1 | | d1 [µm] | d2 [µm] | Δd [%] | HMV1 | | d1 [µm] | d2 [µm] | Δd [%] | | |
| | 376 | 37,6296 | 70,2 | 70,2 | 0,06 | 472 | 47,1703 | 62,7 | 62,7 | 0 | 587,0 | 58,7142 | 56,5 | 55,9 | 1,11 | | |
| | 399 | 39,8711 | 67,7 | 68,7 | 1,53 | 471 | 47,0952 | 62,7 | 62,8 | 0,21 | 592,0 | 59,2388 | 55,8 | 56,1 | 0,56 | | |
| | 374 | 37,4164 | 70,2 | 70,6 | 0,55 | 472 | 47,2459 | 62,5 | 62,8 | 0,48 | 602,0 | 60,2029 | 55,5 | 55,5 | 0,12 | | |
| Average | 383,0 | 38,3 | 69,4 | 69,8 | 0,7 | 471,7 | 47,2 | 62,6 | 62,8 | 0,2 | 593,7 | 59,4 | 55,9 | 55,8 | 0,6 | | |
| | Comment: | | | | | | | | | | | | | | | | |
| | Measurements for HMV0,01 done first on all samples, then HMV0,1, then HMV1 | | | | | | | | | | | | | | | | |
| | 1400 and 1700: Measurements for HMV0,01 done in the middle of the sample, HMV0,1 and HMV1 done a little to the sides | | | | | | | | | | | | | | | | |